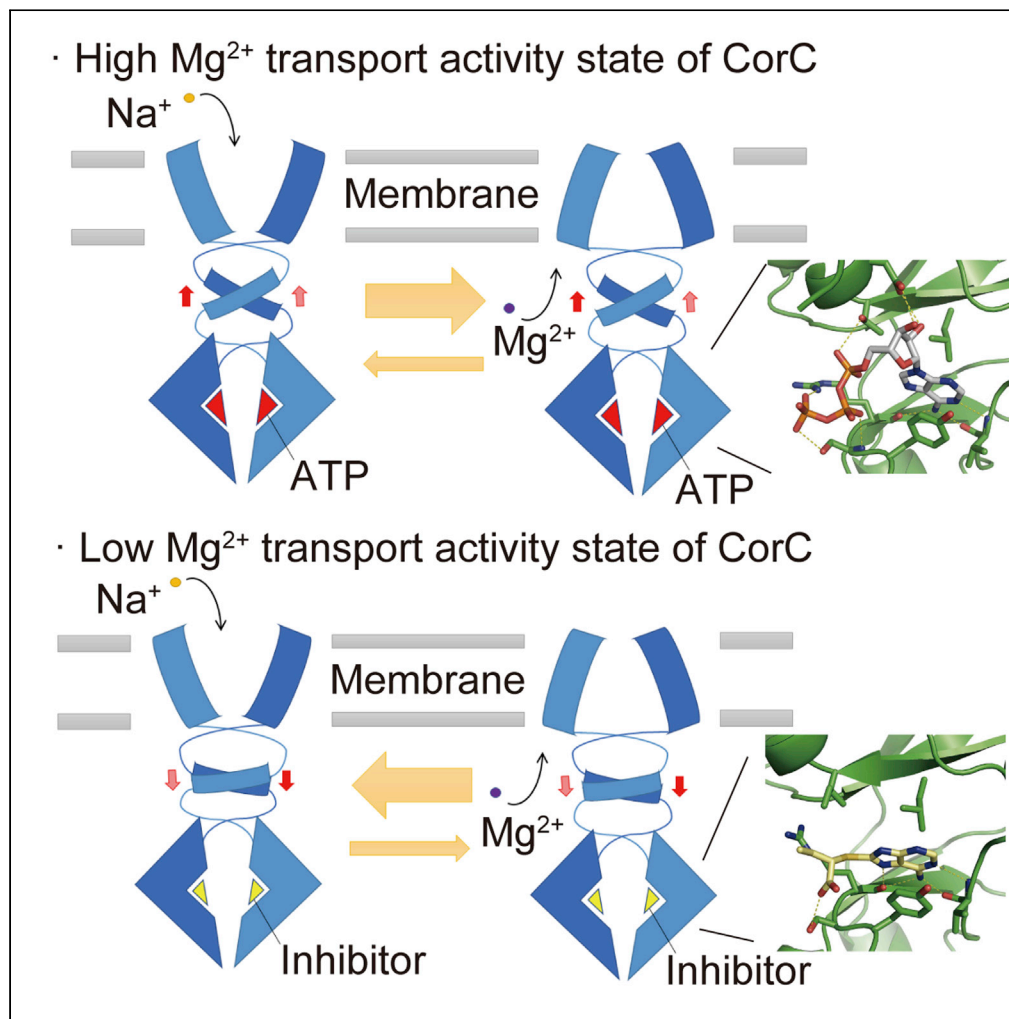


## Article

Identification and mechanistic analysis of an inhibitor of the CorC  $Mg^{2+}$  transporter

Yichen Huang,  
Kaijie Mu, Xinyu  
Teng, ..., Weiliang  
Zhu, Zhijian Xu,  
Motoyuki Hattori

zjxu@simm.ac.cn (Z.X.)  
hattorim@fudan.edu.cn (M.H.)

**Highlights**

A compound, IGN95a,  
inhibited ATP binding and  
 $Mg^{2+}$  export of the CorC  
 $Mg^{2+}$  transporter

The CorC cytoplasmic  
domain structure in  
complex with IGN95a was  
determined

ATP shifted the CorC  
conformational  
equilibrium toward the  
inward-facing state

In contrast, IGN95a  
binding did not induce  
such a shift

Huang et al., iScience 24,  
102370  
April 23, 2021 © 2021 The  
Author(s).  
[https://doi.org/10.1016/  
j.isci.2021.102370](https://doi.org/10.1016/j.isci.2021.102370)

## Article

Identification and mechanistic analysis of an inhibitor of the CorC Mg<sup>2+</sup> transporter

Yichen Huang,<sup>1,4</sup> Kaijie Mu,<sup>2,4</sup> Xinyu Teng,<sup>1,4</sup> Yimeng Zhao,<sup>1</sup> Yosuke Funato,<sup>3</sup> Hiroaki Miki,<sup>3</sup> Weiliang Zhu,<sup>2</sup> Zhijian Xu,<sup>2,\*</sup> and Motoyuki Hattori<sup>1,5,\*</sup>

## SUMMARY

The CorC/CNNM family of Na<sup>+</sup>-dependent Mg<sup>2+</sup> transporters is ubiquitously conserved from bacteria to humans. CorC, the bacterial CorC/CNNM family of proteins, is involved in resistance to antibiotic exposure and in the survival of pathogenic microorganisms in their host environment. The CorC/CNNM family proteins possess a cytoplasmic region containing the regulatory ATP-binding site. CorC and CNNM have attracted interest as therapeutic targets, whereas inhibitors targeting the ATP-binding site have not been identified. Here, we performed a virtual screening of CorC by targeting its ATP-binding site, identified a compound named IGN95a with inhibitory effects on ATP binding and Mg<sup>2+</sup> export, and determined the cytoplasmic domain structure in complex with IGN95a. Furthermore, a chemical cross-linking experiment indicated that with ATP bound to the cytoplasmic domain, the conformational equilibrium of CorC was shifted more toward the inward-facing state of the transmembrane domain. In contrast, IGN95a did not induce such a shift.

## INTRODUCTION

CorC, a prokaryotic member of the CorC/CNNM family of proteins, is involved in Mg<sup>2+</sup> transport (Akanuma et al., 2014; Armitano et al., 2016; Hmiel et al., 1989; Lee et al., 2019; Trachsel et al., 2019). In the pathogenic bacterium *Staphylococcus aureus*, CorC confers resistance to the high concentrations of Mg<sup>2+</sup> ions in the infected host, increasing the pathogenicity of the bacterium (Armitano et al., 2016; Trachsel et al., 2019). Upon exposure to ribosome-targeting antibiotics, the expression of CorC is upregulated in the L22\* strain of *Bacillus subtilis* to enhance Mg<sup>2+</sup> flux for resistance to antibiotics (Lee et al., 2019). Furthermore, in humans, CNNM proteins, eukaryotic members of the CorC/CNNM family of proteins, are involved in a number of biological events, such as body absorption/reabsorption of Mg<sup>2+</sup>, hypertension, genetic disorders, and tumor progression (Funato et al., 2014, 2017; Hardy et al., 2015; Kostantin et al., 2016; Parry et al., 2009; Polok et al., 2009; Stuver et al., 2011; Yamazaki et al., 2013). Therefore, CorC and CNNM are possible targets for novel antibiotics and drugs for treating various diseases, such as cancer. Of note, whether eukaryotic CNNM proteins directly transport Mg<sup>2+</sup> ions or indirectly regulate Mg<sup>2+</sup> transport remains controversial (Arjona and de Baaij, 2018; Funato et al., 2018a, b).

CorC/CNNM family proteins share a conserved transmembrane (TM) DUF21 domain and a cytoplasmic cystathionine-beta-synthase (CBS) domain with the regulatory ATP-binding motif (Armitano et al., 2016; de Baaij et al., 2012; Funato and Miki, 2019; Hmiel et al., 1989). The recently determined structures of the TM and CBS domains of the CorC Na<sup>+</sup>/Mg<sup>2+</sup> antiporter from *Thermus parvatiensis* (TpCorC) revealed the mechanisms of Mg<sup>2+</sup> and ATP binding, respectively (Huang et al., 2021). Subsequently, the crystal structures of CorC from *Methanococcus thermophiles*, containing the TM and CBS domains, were also reported on bioRxiv (Chen et al., 2021). Furthermore, multiple structures containing the CBS domain of CNNM proteins have also been reported thus far (Chen et al., 2018, 2020; Corral-Rodriguez et al., 2014; Gimenez-Mascarell et al., 2019; Gimenez-Mascarell et al., 2017, 2019; Gulerez et al., 2016; Zhang et al., 2017).

The Na<sup>+</sup> gradient is implicated as a driving force for Mg<sup>2+</sup> export from CorC and CNNM (Huang et al., 2021; Yamazaki et al., 2013), whereas ATP binding to the CBS domain of CorC and CNNM proteins is essential for the regulation of Mg<sup>2+</sup> efflux activities (Chen et al., 2020; Hirata et al., 2014; Huang et al., 2021). Therefore,

<sup>1</sup>State Key Laboratory of Genetic Engineering, Collaborative Innovation Center of Genetics and Development, Shanghai Key Laboratory of Bioactive Small Molecules, Department of Physiology and Biophysics, School of Life Sciences, Fudan University, 2005 Songhu Road, Yangpu District, Shanghai 200438, China

<sup>2</sup>CAS Key Laboratory of Receptor Research, Drug Discovery and Design Center, Shanghai Institute of Materia Medica, Chinese Academy of Sciences, 555 Zuchongzhi Road, Pudong New Area, Shanghai, 201203, China

<sup>3</sup>Department of Cellular Regulation, Research Institute for Microbial Diseases, Osaka University, 3-1 Yamadaoka, Suita, Osaka 565-0871, Japan

<sup>4</sup>These authors contributed equally

<sup>5</sup>Lead contact

\*Correspondence: zjxu@simm.ac.cn (Z.X.), hattorim@fudan.edu.cn (M.H.)

<https://doi.org/10.1016/j.isci.2021.102370>



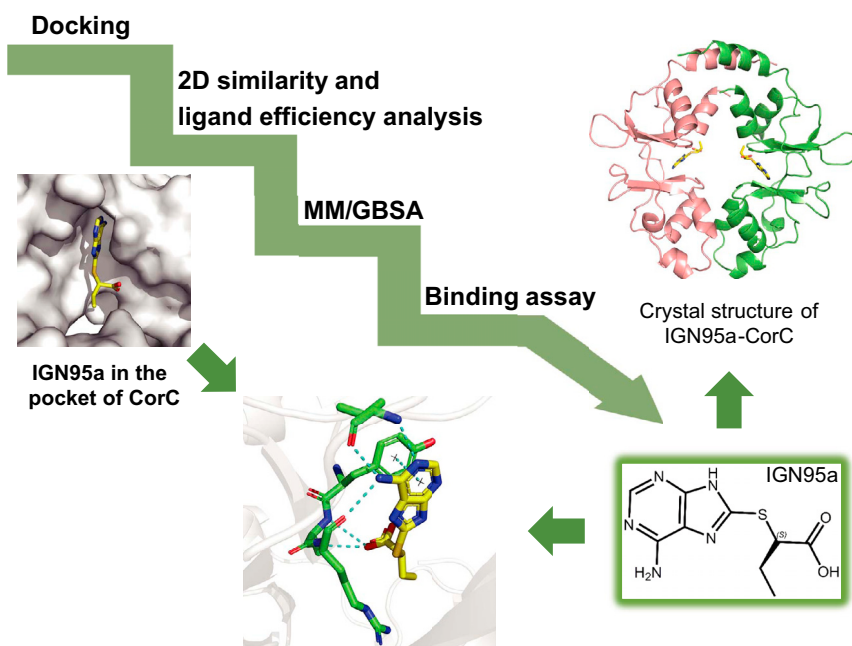


**Figure 1. Computational strategy to identify active compounds**

Molecular docking, 2D similarity analysis, atom efficiency analysis, and MM/GBSA calculations were combined to identify active compounds against CorC.

chemical compounds targeting the CBS domain of the CorC/CNNM family proteins, especially their ATP-binding site, could be exploited for therapeutic interventions against various diseases, but such compounds have not yet been identified, hindering the development and optimization of chemical compounds targeting the CorC and CNNM proteins. Furthermore, how ATP binding to CorC and CNNM proteins modulates their transport activity also remains unclear.

In this work, based on the ATP-bound structure of the CorC CBS domain, we performed virtual screening and functional assays to identify chemical compounds targeting the ATP-binding site of the CorC CBS domain and identified the chemical compound with inhibitory effects on ATP binding and  $Mg^{2+}$  export. Structural and biochemical analyses provided mechanistic insights for further design and optimization of chemical compounds targeting the ATP-binding site of CorC as well as mechanistic insights into how ATP and chemical compounds modulate the transport activity of CorC.

## RESULTS

### Virtual screening

A computational strategy was applied to find potential active compounds against CorC (Figure 1). First, 6,412 compounds designed in-house were docked to the ATP-binding site in the CorC CBS domain structure (PDB ID: 7CFI). Then, 12 docked compounds among the compounds with the top 30 2D similarities with ligand efficiencies better than  $-0.40$  kcal/mol, which interacted with at least three residues in the pocket via hydrogen bonds and  $\pi$ - $\pi$  interactions, were chosen for further molecular mechanics with generalized Born and surface area solvation (MM/GBSA) calculations (Figure 2 and Table 1). As shown in Table 2, three available compounds (IGN95a, IGN23, and IGN19) with binding free energies greater than  $-10$  kcal/mol were selected for the bioassay.

### In vitro screening

We then performed fluorescent ATP-based binding assays with the chemical compound candidates from the virtual screening. We employed 2'(3')-O-(N-methylanthraniloyl)adenosine 5'-triphosphate (mant-ATP) for the binding assay and measured fluorescence resonance energy transfer (FRET) from endogenous Trp residues to the bound mant-fluorophore (Göttle et al., 2007; Ni et al., 2000).

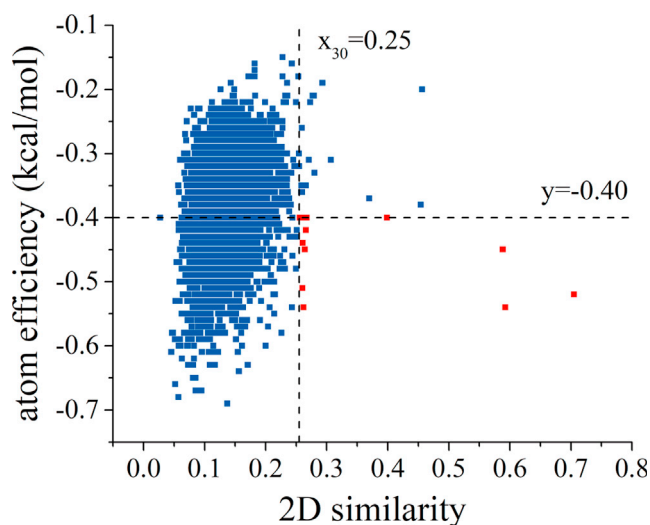


**Figure 2. Compound selection from 2D similarity and atom efficiency analysis**

The top 30 compounds with the highest 2D similarity to ATP were selected first. Among them, 12 compounds with atom efficiencies better than  $-0.40$  (colored red) were chosen for further MM/GBSA calculations.

The FRET data showed that mant-ATP was bound to the purified CorC CBS domain with a  $K_d$  of  $1.36 \pm 0.10 \mu\text{M}$  (Figure 3A). For validation of this method, we performed a competitive binding assay with ATP (Figure 3B). The addition of ATP at the respective concentrations yielded an  $\text{IC}_{50}$  value of  $0.57 \pm 0.08 \mu\text{M}$ , which is comparable with the previously reported  $K_d$  value of the CorC CBS domain for ATP obtained by isothermal titration calorimetry (ITC) (Huang et al., 2021).

Finally, from the mant-ATP-based screening of chemical compound candidates from the virtual screening, we identified IGN95a, an adenine analog, as the compound that most potently inhibited mant-ATP binding (Figures 3C and 3D).

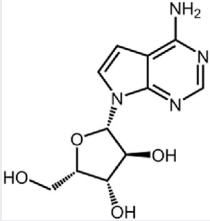
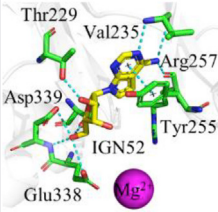
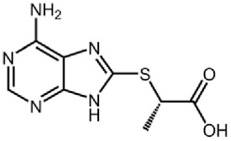
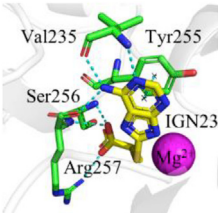
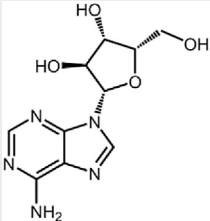
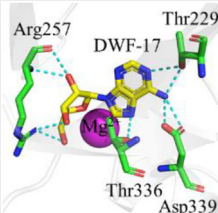
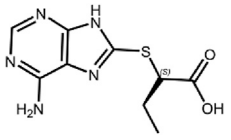
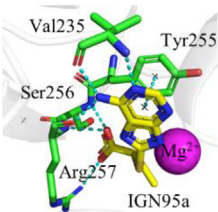
### Characterization of IGN95a

We further characterized IGN95a (Figure 4). First, the ITC experiment confirmed IGN95a binding to the CorC CBS domain with a  $K_d$  value of  $47.0 \mu\text{M}$  (Figures 4A and Table S1). Notably, we did not exclude the possibility that the estimated  $K_d$  might be affected by the partially unremoved ATP in the purified protein to some extent given that the wild-type CBS domain protein exhibits high affinity for ATP ( $\sim 500 \text{ nM}$ ) (Huang et al., 2021).

We then tested the effects of IGN95a on the  $\text{Mg}^{2+}$  export activity of CorC (Figure 4B). We performed  $\text{Mg}^{2+}$  export activity assay with Magnesium Green, a fluorescent  $\text{Mg}^{2+}$  indicator dye that has a wide dynamic range and is well suited for sensitively monitoring the change in  $\text{Mg}^{2+}$  levels in time-lapse analyses. We employed the human embryonic kidney 293 (HEK293) cell line stably expressing CorC at the cell surface, as it was employed for the previous structure-based mutational analysis of CorC (Huang et al., 2021). The intensity of the fluorescent signal in the control cells expressing CorC soaked with a buffer containing only 1% DMSO decreased after the removal of  $\text{Mg}^{2+}$  ions from the bath solution, whereas we observed inhibitory effects of IGN95a on the  $\text{Mg}^{2+}$  export activity of CorC after soaking with IGN95a in 1% DMSO buffer with HEK293 cells expressing CorC (Figure 4B). These results show that IGN95a acts as an inhibitor of both ATP binding and  $\text{Mg}^{2+}$  export, and also indicates that IGN95a can permeate the mammalian cell membrane. Consistently, the computationally calculated  $\text{miLogP}$  value of 1.26 also suggested the cell membrane permeability of IGN95a. Thus, considering the  $\text{miLogP}$  value and mammalian cell permeability, we hypothesize that IGN95a can also likely permeate the bacterial cell membrane.

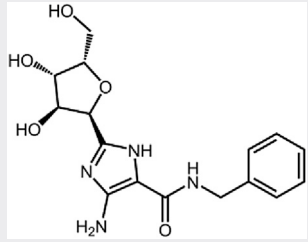
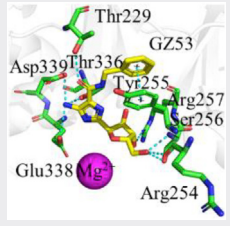
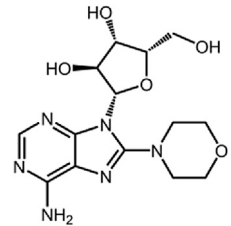
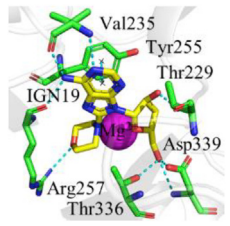
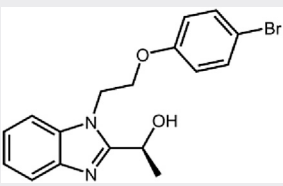
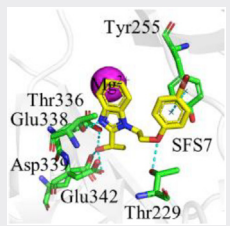
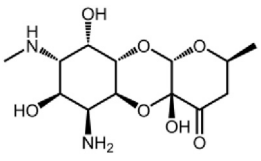
Furthermore, we tested IGN95a binding to the CBS domain of human CNNM2 and CNNM4 (Figures 4C and 4D). In the ITC experiments, IGN95a showed weak binding to CNNM2 and CNNM4. The exact  $K_d$  values could not be estimated because the titrations were not completed ( $>1,000 \mu\text{M}$  for the CBS domain of CNNM2,  $>500 \mu\text{M}$  for the CBS domain of CNNM4). To estimate the exact  $K_d$  values, other methods with

**Table 1. Twelve compounds selected are ranked by atom efficiency**

Molecule name	Chemical structure	Docking score (kcal/mol)	2D similarity	Atom efficiency	Interaction diagrams in docked models
IGN52		-10.22	0.59	-0.54	
IGN23		-8.61	0.26	-0.54	
DWF-17		-9.83	0.71	-0.52	
IGN95a		-8.65	0.26	-0.51	

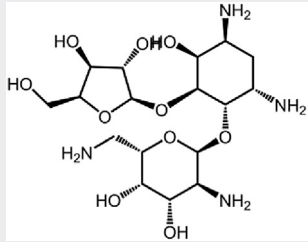
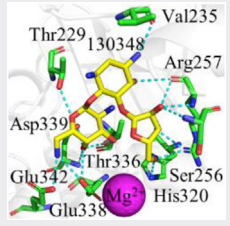
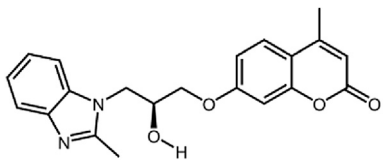
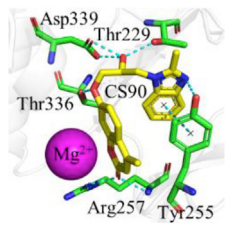
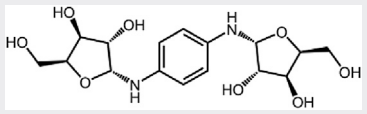
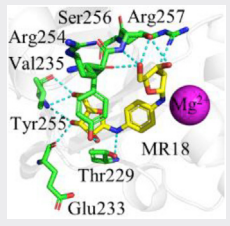
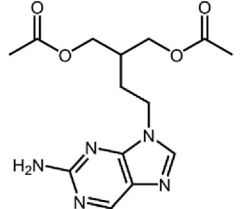
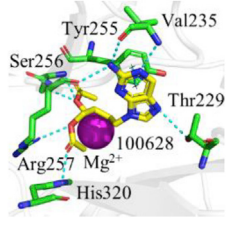
(Continued on next page)

Table 1. Continued

Molecule name	Chemical structure	Docking score (kcal/mol)	2D similarity	Atom efficiency	Interaction diagrams in docked models
GZ53		-11.34	0.26	-0.45	
IGN19		-11.33	0.59	-0.45	
SFS7		-9.58	0.26	-0.44	
130354		-9.59	0.27	-0.42	

(Continued on next page)

Table 1. Continued

Molecule name	Chemical structure	Docking score (kcal/mol)	2D similarity	Atom efficiency	Interaction diagrams in docked models
130348		-12.32	0.26	-0.40	
CS90		-10.75	0.26	-0.40	
MR18		-10.35	0.27	-0.40	
100628		-9.26	0.40	-0.40	

**Table 2. The binding free energies of 12 compounds to TpCorC calculated by MM/GBSA**

Molecule name	$E_{vdw}$	$E_{ele}$	$E_{gb}$	$E_{surf}$	$\Delta H$	$-T\Delta S$	$\Delta G_{cal}$
IGN95a	-28.51 ±0.31	196.87 ±2.60	-194.94 ±2.30	-4.17 ±0.02	-30.75 ±0.54	16.87 ±0.95	-13.88 ±1.49
IGN23	-27.90 ±0.28	198.84 ±4.89	-197.55 ±4.26	-3.93 ±0.02	-30.54 ±0.70	17.17 ±2.16	-13.37 ±2.86
GZ53	-41.53 ±0.27	-41.91 ±1.63	53.06 ±1.49	-5.75 ±0.02	-36.13 ±0.38	24.63 ±0.84	-11.5 ±1.22
IGN19	-35.94 ±0.37	-46.84 ±1.46	52.22 ±1.28	-4.64 ±0.03	-35.21 ±0.68	24.91 ±3.37	-10.3 ±4.05
100628	-35.18 ±0.25	-26.07 ±0.63	35.57 ±0.56	-4.46 ±0.02	-30.14 ±0.26	20.06 ±0.46	-10.08 ±0.72
SFS7	-33.49 ±0.30	9.04 ±1.33	9.05 ±1.23	-4.52 ±0.03	-19.93 ±0.33	13.64 ±2.22	-6.29 ±2.55
IGN52	-28.90 ±0.25	-36.99 ±1.25	44.28 ±1.10	-3.89 ±0.02	-25.49 ±0.29	20.73 ±3.26	-4.76 ±3.55
CS90	-34.96 ±0.24	-33.75 ±0.62	50.82 ±0.55	-4.75 ±0.03	-22.64 ±0.31	20.02 ±1.02	-2.62 ±1.33
DWF-17	-31.65 ±0.25	-22.05 ±1.34	33.86 ±1.02	-4.05 ±0.03	-23.89 ±0.58	21.87 ±3.11	-2.02 ±3.69
MR18	-28.10 ±0.48	-68.92 ±1.57	73.54 ±1.29	-5.15 ±0.04	-28.64 ±0.53	27.53 ±0.82	-1.11 ±1.35
130348	-11.48 ±0.57	-1,684.72 ±5.22	1,668.17 ±5.27	-4.54 ±0.03	-32.58 ±0.60	31.56 ±1.38	-1.02 ±1.98
130354	-7.01 ±0.32	-940.06 ±2.86	928.9 ±2.68	-2.49 ±0.03	-20.68 ±0.50	19.92 ±0.73	-0.76 ±1.23

$E_{vdw}$ : the van der Waals energy contribution;  $E_{ele}$ : the electrostatic energy contribution;  $E_{gb}$ : electrostatic contribution to the solvation free energy;  $E_{surf}$ : non-polar energy contribution to the solvation free energy;  $\Delta H = E_{vdw} + E_{ele} + E_{gb} + E_{surf}$ ;  $T\Delta S$ : the entropy changes;  $\Delta G_{cal}$ : the binding free energy between each compound and TpCorC.

a higher dynamic range of dissociation constants, such as microscale thermophoresis, can be potentially applicable.

Overall, these results suggest the specificity of IGN95a against CorC compared with CNNM family proteins. Given that CNNM2 and CNNM4 mutations are associated with human genetic diseases, including dominant hypomagnesemia (Stuiver et al., 2011) and Jalili syndrome (Parry et al., 2009; Polok et al., 2009), the specificity of IGN95a against CorC compared with CNNM family proteins may be beneficial for future optimization to avoid side effects *in vivo*.

### Inhibitor-bound structure

To understand the molecular interactions between the CorC CBS domain and IGN95a, we performed co-crystallization of the TpCorC CBS domain with IGN95a.

As the wild-type CBS domain protein has a very high affinity for ATP, it was difficult to completely remove endogenous ATP during purification, which is not ideal for co-crystallization with IGN95a. Therefore, we employed the T336I mutant with weaker affinity for ATP (Huang et al., 2021) because mutation at Thr336 was relatively unlikely to affect IGN95a binding based on the initial docking model. Indeed, we successfully determined the crystal structure of the TpCorC CBS domain in complex with IGN95a (Figures 5A and S1).

The adenine ring of IGN95a is recognized by the TpCorC domain (Figure 5A), similar to ATP (Figure 5B). One of the oxygen groups forms an additional hydrogen bond with the side chain of Ser256 (Figures 5A and 5C). In the ATP-bound structure, Thr336, Glu338, and Asp339 form multiple hydrogen bonds with ATP (Figure 5B), but the corresponding residues are not involved in direct interactions with IGN95a (Figure 5A).

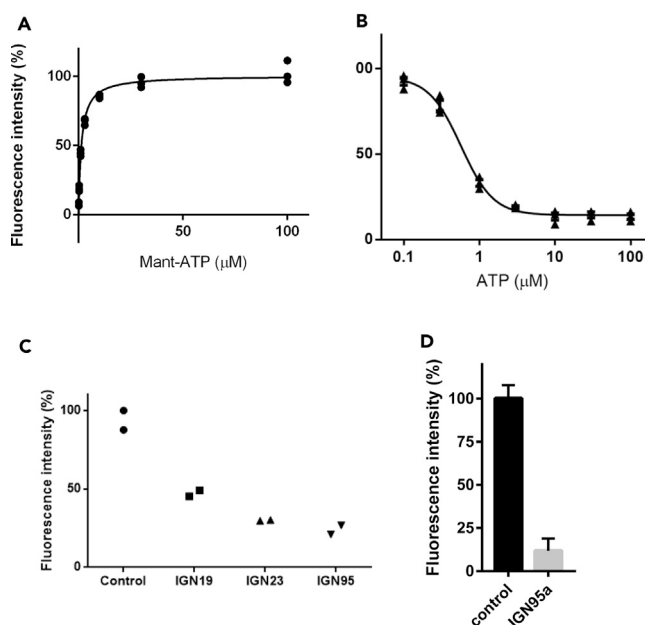


**Figure 3. Mant-ATP binding assay**

(A) Saturation of mant-ATP binding to the CorC CBS domain (1  $\mu\text{M}$ ) detected by FRET. Data are expressed as the mean  $\pm$  SE.  $R^2 = 0.9989$ ,  $n = 3$ .

(B) ATP-based inhibition test of the binding of the CorC CBS domain (1  $\mu\text{M}$ ) and mant-ATP (1  $\mu\text{M}$ ) using FRET. Data are expressed as the mean  $\pm$  SE.  $R^2 = 0.9894$ ,  $n = 3$ .

(C and D) Mant-ATP binding inhibition by chemical compounds. (C) Data are expressed as dots.  $n = 2$ . Each chemical compound was added at 0.25 mM. (D) Data are expressed as the mean  $\pm$  SE.  $n = 6$ . IGN95a was added at 2 mM.

The binding pose of IGN95a with CorC in the crystal structure is similar to the docking pose, including the same  $\pi$ - $\pi$  interaction with Tyr255 (Figures S2A and S2B). To examine the stability of the binding of IGN95a to CorC, explicit-solvent molecular dynamics (MD) simulation of the crystal structure of the CorC CBS domain in complex with IGN95a was performed. The representative conformation of the largest clusters of the 300-ns trajectories for IGN95a have similar interactions with the key residues (Val235, Tyr255, and Arg257) in the crystal structure (Figures 5A and S3A). Compared with the initial structure, the root-mean-square deviations for IGN95a range from 0.2  $\text{\AA}$  to 1.5  $\text{\AA}$  (Figure S3B), and the key interactions exist during the 300-ns MD simulations (Figures S3C and S3D), implying that IGN95a is stable in the binding pocket.

To further verify the structure, we performed a binding assay of the ATP-binding site mutants Y255A (adenine ring) and T336I (ribose) using ITC. According to the structure, mutation at Tyr255 should severely affect IGN95a binding, whereas mutation at Thr336 should have a weaker impact on IGN95a binding (Figure 5A). The T336I mutant of the CBS domain exhibited a  $K_d$  value of 147.3  $\mu\text{M}$  for IGN95a, whereas there were no detectable interactions between the Y255A mutant and IGN95a (Figures 5D and 5E, and Table S1), essentially supporting our structure. The POLDER-OMIT maps showed clear electron densities for most parts of IGN95a, except for the one for the ethyl group (Figure S1). Consistently, the ethyl group of IGN95a seems to exhibit no direct interactions with the CorC CBS domain, and would be exposed to the exterior of the ATP-binding pocket (Figure 5A). Thus, this part of IGN95a might be a promising modification target for further optimization of chemical compounds.

### Effect of ATP and IGN95a on the structural equilibrium of the CorC TM domain

To gain insights into the ATP modulation and IGN95a inhibition mechanisms of CorC, we performed biochemical cross-linking experiments using the cross-linking mutant of TpCorC (Figure 6), which we established previously (Huang et al., 2021). The TM domain of TpCorC adopts an inward-facing conformation in the presence of  $\text{Mg}^{2+}$ , with an inter-subunit distance of 7.1  $\text{\AA}$  between the  $\text{C}\beta$  atoms of Thr106 residues (Figure 6A), which is sufficiently close for chemical cross-linking through Cys residues. We previously generated the cross-linking mutant of TpCorC (T106C/C282A), where Cys282 was also mutated to remove an endogenous cysteine residue. In fact, previous cross-linking experiments with  $\text{Cu}^{2+}$  phenanthroline

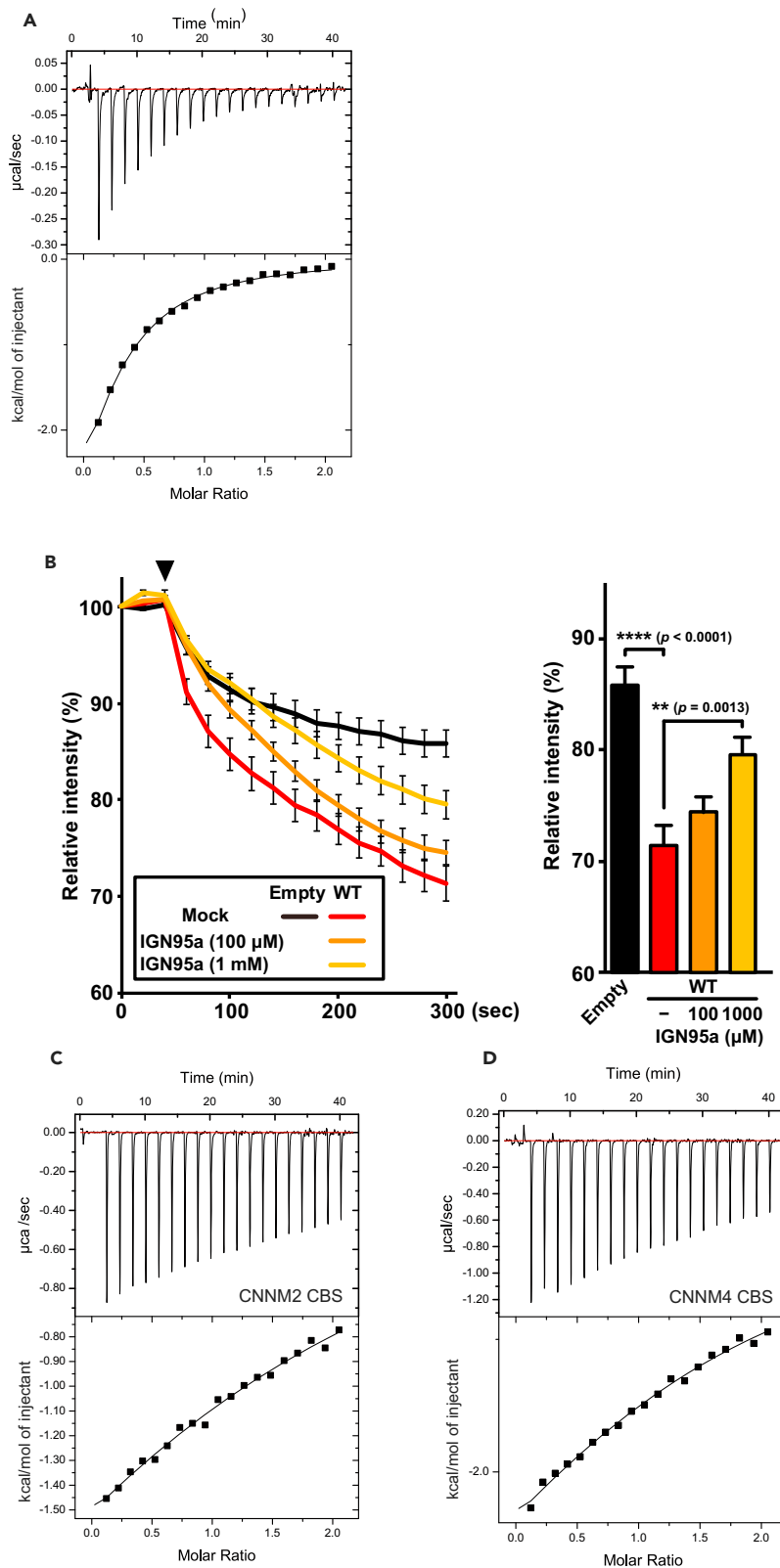


**Figure 4. Functional characterization of IGN95a**

(A) ITC data of the TpCorC CBS domain with IGN95a. The raw ITC data and profiles are shown. Measurements were repeated twice, and similar results were obtained.  
 (B)  $Mg^{2+}$  export assay of CorC-expressing cells treated with IGN95a. Line graph: time course of mean relative fluorescent intensities.  $Mg^{2+}$  was depleted at the time point indicated with an arrowhead. Bar graph: relative fluorescence intensities after  $Mg^{2+}$  depletion at 5 min. The data are shown as mean  $\pm$  SEM (Empty: n = 10, WT without IGN95a: n = 18, WT with 100  $\mu$ M IGN95a: n = 19, and WT with 1,000  $\mu$ M IGN95a: n = 30).  
 (C and D) ITC data of the CBS domain of CNNM2 (C) and CNNM4 (D) with IGN95a.

showed that the T106C pair of TpCorC formed a disulfide bond in the presence of  $Mg^{2+}$ , as indicated by a strong band for the dimer on a non-reducing SDS-PAGE gel (Huang et al., 2021) (Figure 6B). Furthermore, whereas the addition of  $Na^+$  disrupted the cross-linked dimer, the replacement of  $Na^+$  with  $K^+$  resulted in bands for both the TpCorC monomer and dimer (Huang et al., 2021) (Figure 6B).

Intriguingly, the addition of ATP to the TpCorC cross-linking mutant in the absence of  $Na^+$  and  $Mg^{2+}$  led to a stronger dimer band than that of the ATP-free sample in the absence of  $Na^+$  and  $Mg^{2+}$  (Figure 6B), whereas we did not see such a shift upon the addition of IGN95a (Figure 6B). Based on this result, we hypothesized that ATP binding to the TpCorC CBS domain affects the conformational equilibrium of the TM domain toward more inward-facing conformations.

To further verify this hypothesis, we generated an ATP-binding site mutant of the TpCorC cross-linking construct (T106C/C282A/Y255A/T336I) for chemical cross-linking experiments (Figure 6B). Mutations in Y255A/T336I are known to abolish the ATP-binding activity of TpCorC as well as lower  $Mg^{2+}$  export activity (Huang et al., 2021). As expected, the addition of ATP to this mutant did not lead to a stronger dimer band than that of the original cross-linking mutant (Figure 6B), further supporting our hypothesis regarding the effect of ATP on TpCorC. Notably, because the TpCorC CBS domain has no ATP hydrolysis activity (Huang et al., 2021), ATP binding would be sufficient to affect the conformational equilibrium of the TM domain.

**DISCUSSION**

In this work, we performed virtual and *in vitro* screening of CorC by targeting its ATP-binding site and identified a chemical compound, IGN95a, with inhibitory effects on both the ATP binding and  $Mg^{2+}$  export activities of CorC (Figures 1, 2, 3, and 4). Co-crystallization of the CorC ATP-binding domain with IGN95a and associated MD simulations provided structural insights for the further development and optimization of chemical compounds for the CorC ATP-binding site (Figure 5). Finally, chemical cross-linking experiments indicate that ATP binding to the CorC CBS domain shifts the conformational equilibrium of its TM domain toward more inward-facing conformations, whereas IGN95a, which occupies the ATP-binding site, does not have such an effect (Figure 6). Based on these results, we discuss the mechanisms of action of ATP and IGN95a on CorC (Figures 7 and 8)

First, a comparison of the apo, IGN95a-bound, and ATP-bound structures of the CBS domain suggests that the IGN95a-bound structure is more similar to the apo structure than to the ATP-bound structure (Figure 7). In the ATP-bound structure, the helix region on the exterior of the ATP-binding site moves slightly outward from the pocket, mainly via its contact with the ribose moiety of ATP (Figure 7B). In contrast, IGN95a binding did not induce such movement (Figure 7A). Previous chemical cross-linking experiments and MD simulations suggested that this region, undergoing this ATP-dependent structural change, is located at the interface between the TM and CBS domains (Huang et al., 2021) (Figure S4). Consistent with this, our chemical cross-linking experiments indicated that ATP binding to the CorC CBS domain affects the conformational equilibrium of the TM domain, shifting it toward more inward-facing conformations (Figures 6 and 8), which would be more favorable for attraction of intracellular  $Mg^{2+}$  to the  $Mg^{2+}$ -binding pocket in the TM domain. As the transport activity of CorC is lower in the absence of ATP binding (Huang et al., 2021), the ATP-dependent structural change in the CBS domain might be important for CorC to properly maintain its transport activity by adjusting the structural equilibrium of CorC toward a more inward-facing state through the contacts between the TM and CBS domains (Figures 8A and 8B). Notably, the binding of ATP to the CBS domain of the CIC-1  $Cl^-$  channel also affects its transport activity through the domain interface between the TM and CBS domains (Wang et al., 2019). In contrast, the binding of IGN95a to the ATP-binding site does not induce the

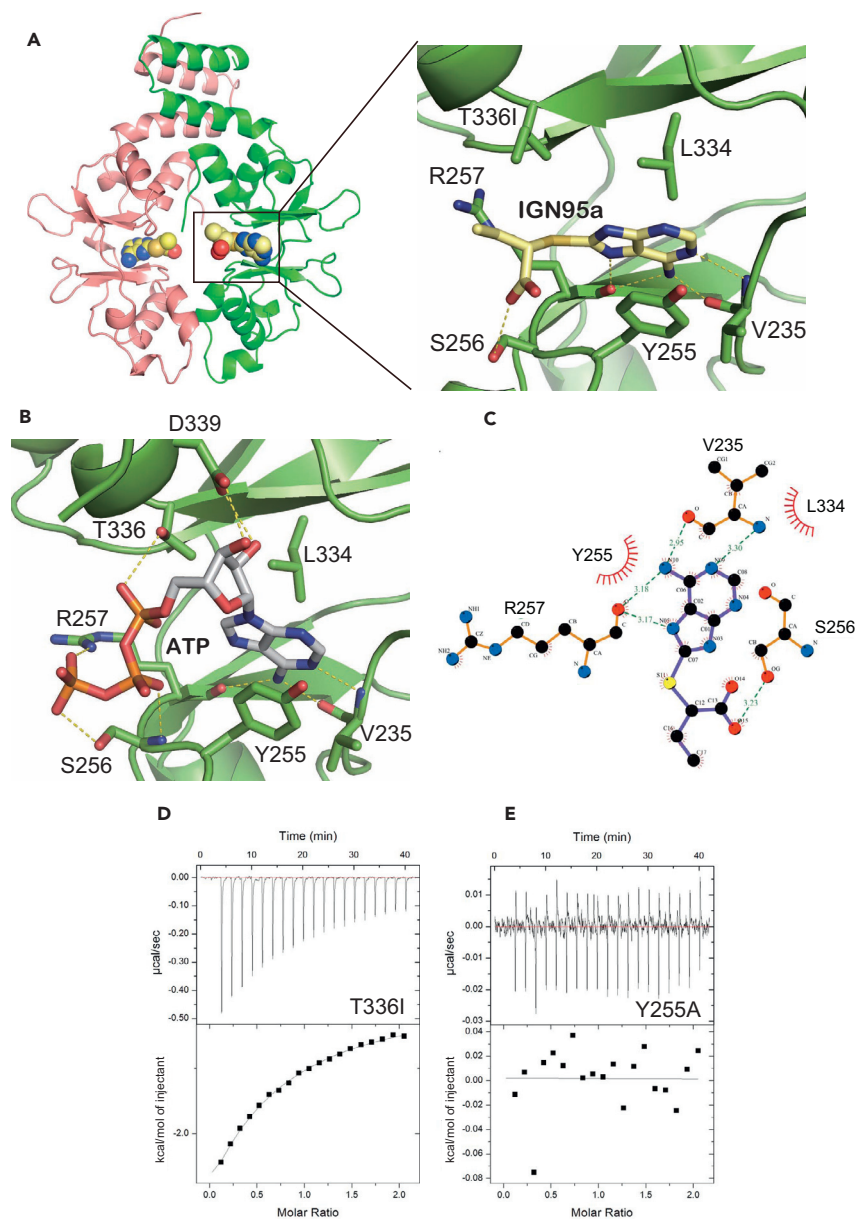


**Figure 5. IGN95a-bound structure of the CorC CBS domain**

(A and B) Close-up views of the IGN95a-binding (A) and ATP-binding (B) sites in the CorC CBS domain. Ligands and the surrounding residues are shown in stick representation. Dashed lines indicate hydrogen bonds.

(C) 2D interaction diagram between IGN95a and the CorC CBS domain.

(D and E) ITC data of CorC CBS domain mutants with IGN95a. The raw ITC data and profiles are shown. Measurements were repeated twice, and similar results were obtained.

ATP-dependent conformational change of the CBS domain at the interface between the TM and CBS domains (Figures 7, 8C, and S4). Considering the affinity of the CorC CBS domain for ATP (Huang et al., 2021) and the cytoplasmic ATP concentration (~1 mM) (Beis and Newsholme, 1975; Yaginuma et al., 2014), CorC would be mostly in the ATP-bound form *in vivo*. Thus, the addition of IGN95a lowers the transport activity of CorC (Figure 4B), probably because IGN95a binding inhibits the binding of ATP in a competitive manner (Figure 5) and inhibits the associated structural changes (Figure 7), which in turn prevents the adjustment of the conformational equilibrium of the TM domain (Figures 6 and 8).

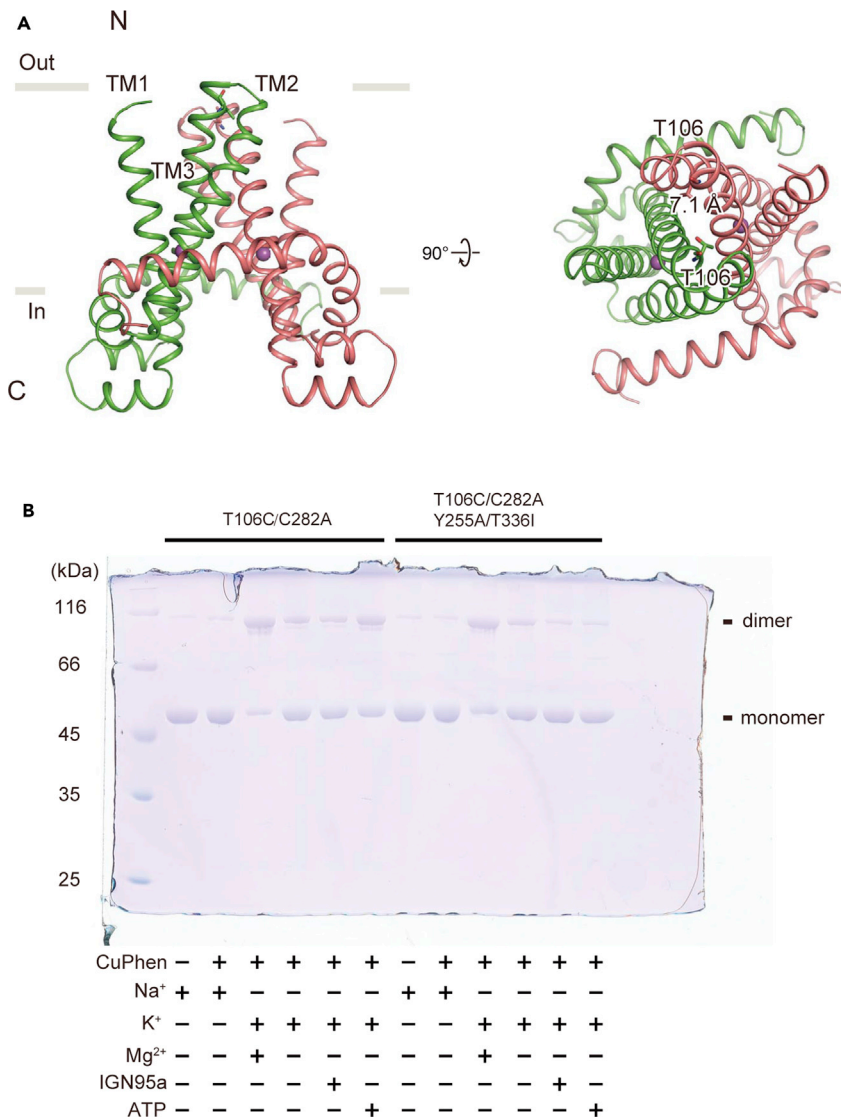


**Figure 6. Inter-subunit chemical cross-linking of CorC with ATP and IGN95a**

(A) Structure of the TpCorC TM domain dimer (PDB ID: 7CFF) in cartoon representation, viewed parallel to the cell membrane (left) and from the periplasmic side (right). The Thr106 residues are depicted in stick representation. Dashed lines show the C $\alpha$  distances between the Thr106 residues within the dimer.

(B) Chemical cross-linking experiments of the inter-subunit cross-linking mutant (T106C/C282A) of TpCorC and its ATP-binding site mutant (T106C/T255A/C282A/T336I).

### Limitations of the study

Notably, whether eukaryotic CNNM proteins directly transport Mg<sup>2+</sup> ions or regulate Mg<sup>2+</sup> transport remains controversial (Arjona and de Baaij, 2018; Funato et al., 2018a, 2018b). Given that this study focuses on bacterial CorC, this controversy does not affect our main conclusion. To settle the controversy, additional Mg<sup>2+</sup> transport assays of eukaryotic CNNM proteins, particularly purified proteins in liposomes, should be performed, but these experiments are beyond the scope of this study. Furthermore, whereas IGN95a inhibited Mg<sup>2+</sup> export activities of CorC in HEK293 cells, further characterization on Mg<sup>2+</sup> export activities, particularly experiments using the bacterial system, are also required in the future.

Overall, our results provide not only structural insights for the further design and optimization of chemical compounds targeting the ATP-binding site of CorC but also mechanistic insights into how ATP and chemical compounds modulate the transport activity of CorC.

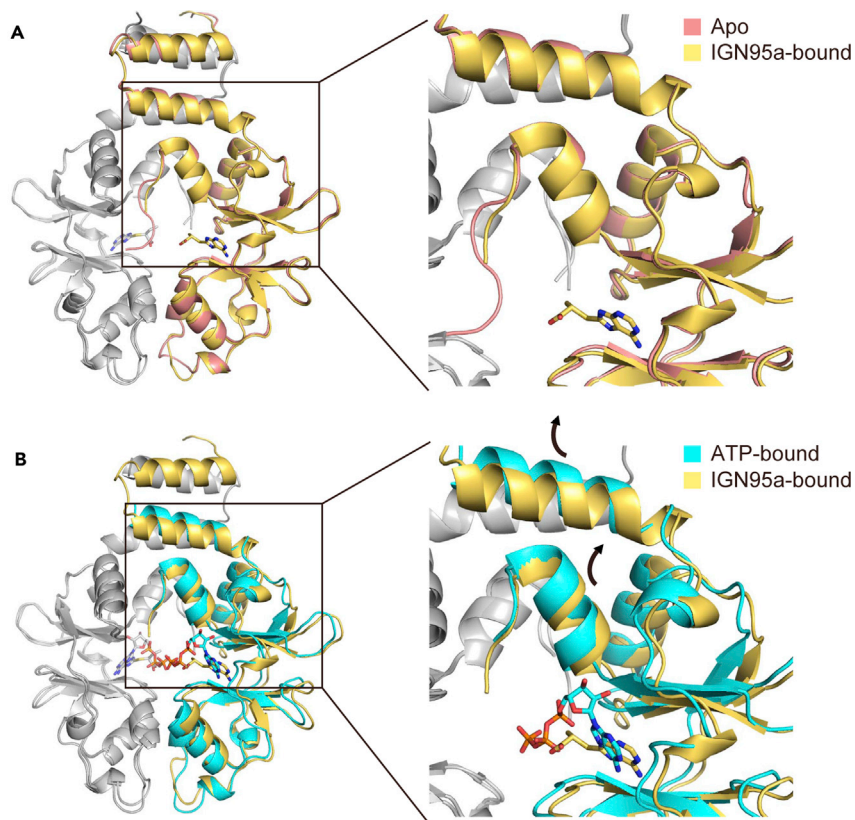


**Figure 7. Structural comparisons of the apo, ATP-bound, and IGN95a-bound structures of the CorC CBS domain**  
(A) Superposition of the IGN95a-bound CBS domain structure (yellow) onto the apo structure (red).  
(B) Superposition of the ATP-bound CBS domain structure (cyan) onto the IGN95a-bound structure (yellow). Both subunits in the dimer are shown, and the neighboring subunit of the dimer is colored gray. Both the overall structure and close-up view of the region near the exterior of the ATP-binding site are shown. Black arrows indicate the structural changes between two conformations.

### Resource availability

#### Lead contact

Further information and requests for resources and reagents should be directed to and will be fulfilled by the lead contact, Motoyuki ([hattorim@fudan.edu.cn](mailto:hattorim@fudan.edu.cn)).

#### Materials availability

Plasmids and other materials generated in this study can be requested from the lead contact, Motoyuki Hattori ([hattorim@fudan.edu.cn](mailto:hattorim@fudan.edu.cn)).

#### Data and code availability

The atomic coordinates and structural factors for the structure of the CorC CBS domain in the IGN95a-bound form have been deposited in the Protein DataBank under accession code 7CFK.

### METHODS

All methods can be found in the accompanying [transparent methods supplemental file](#).

### SUPPLEMENTAL INFORMATION

Supplemental information can be found online at <https://doi.org/10.1016/j.isci.2021.102370>.

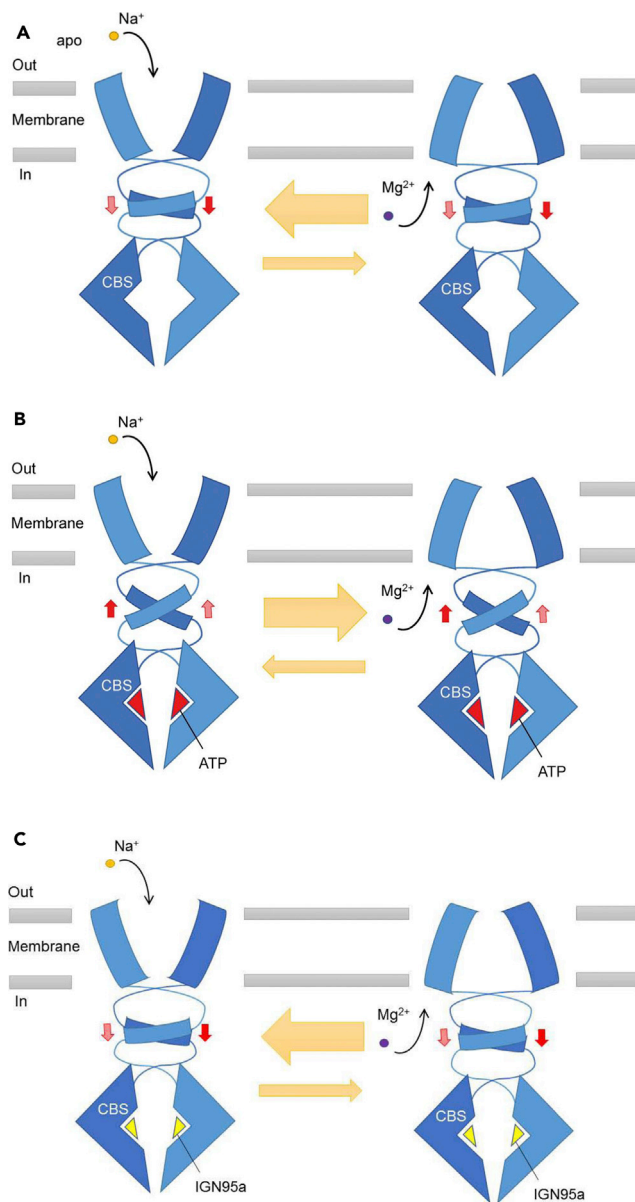


**Figure 8. Proposed CorC regulation mechanisms by ATP and IGN95a**

(A–C) Schematic diagrams of the conformational equilibrium of the CorC in the apo (A), ATP-bound (B), and IGN95a-bound (C) forms. ATP binding induces structural changes in the cytoplasmic domain at the interface between the TM and cytoplasmic domains, which shifts the conformational equilibrium of the transmembrane domain more toward the inward-facing state (A and B). In contrast, IGN95a binding inhibits the binding of ATP in a competitive manner and inhibits the associated structural changes, which in turn prevents the adjustment of the conformational equilibrium of the TM domain (C).  $Mg^{2+}$  and  $Na^+$  ions are shown as purple and orange spheres, respectively. Black arrows indicate the metal transport directions.

## ACKNOWLEDGMENTS

We thank the staff from the BL32XU beamline at SPring-8 and from the BL17U1 beamline at Shanghai Synchrotron Radiation Facility (SSRF) for their assistance during data collection. The diffraction experiments were performed at SPring-8 BL32XU (proposal no. 2019A2514) and at SSRF BL17U1 (proposal no. 2018-SSRF-PT-004257). This work was supported by funding provided by the Ministry of Science and Technology of the People's Republic of China (National Key R&D Program of China: 2016YFA0502800) to M.H., by

funding provided by the National Natural Science Foundation of China (32071234), and by funding provided by the Innovative Research Team of High-level Local Universities in Shanghai and a key laboratory program of the Education Commission of Shanghai Municipality (ZDSYS14005). This work was also supported by funding provided by the Japan Society for the Promotion of Science to H.M. (JP26111007, JP17H04041, and JP20H03515) and to Y.F. (JP20K07312, JP20H05508, and JP17K19396).

## AUTHOR CONTRIBUTIONS

Y.H. and X.T. expressed and purified CorC and its mutants for structural and functional studies and determined the structure. Y.H. and X.T. performed the ITC, and Y.H. and X.T. conducted biochemical cross-linking experiments. Y.F. performed the  $Mg^{2+}$  export assay. Z.X., K.M., and W.Z. performed the virtual screening and MD simulations. Y.H. and Y.Z. performed the binding assays for chemical compounds. Y.H., Z.X., K.M., Y.F., H.M., and M.H. wrote the manuscript. Z.X. and M.H. supervised the research. All authors discussed the manuscript.

## DECLARATION OF INTERESTS

The authors declare no competing interests.

Received: February 2, 2021

Revised: March 17, 2021

Accepted: March 24, 2021

Published: April 23, 2021

## REFERENCES

- Akanuma, G., Kobayashi, A., Suzuki, S., Kawamura, F., Shiwa, Y., Watanabe, S., Yoshikawa, H., Hanai, R., and Ishizuka, M. (2014). Defect in the formation of 70S ribosomes caused by lack of ribosomal protein L34 can be suppressed by magnesium. *J. Bacteriol.* 196, 3820–3830.
- Arjona, F.J., and de Baaij, J.H.F. (2018). CrossTalk opposing view: CNNM proteins are not  $Na^+$ / $Mg^{2+}$  exchangers but  $Mg^{2+}$  transporter regulators playing a central role in transepithelial  $Mg^{2+}$  (re) absorption. *J. Physiol.* 596, 747–750.
- Armitano, J., Redder, P., Guimaraes, V.A., and Linder, P. (2016). An essential factor for high  $Mg^{2+}$  Tolerance of *Staphylococcus aureus*. *Front. Microbiol.* 7, 1888.
- Beis, I., and Newsholme, E.A. (1975). The contents of adenine nucleotides, phosphagens and some glycolytic intermediates in resting muscles from vertebrates and invertebrates. *Biochem. J.* 152, 23–32.
- Chen, Y.S., Kozlov, G., Armitano, J., Moeller, B.E., Fakhri, R., Rohaim, A., Roux, B., Burke, J.E., and Gehring, K. (2021). Crystal structure of a bacterial CNNM magnesium transporter. *bioRxiv*2021.02.11.430706. <https://doi.org/10.1101/2021.02.11.430706>.
- Chen, Y.S., Kozlov, G., Fakhri, R., Funato, Y., Miki, H., and Gehring, K. (2018). The cyclic nucleotide-binding homology domain of the integral membrane protein CNNM mediates dimerization and is required for  $Mg^{2+}$  efflux activity. *J. Biol. Chem.* 293, 19998–20007.
- Chen, Y.S., Kozlov, G., Fakhri, R., Yang, M., Zhang, Z., Kovrigin, E.L., and Gehring, K. (2020).  $Mg^{2+}$ -ATP sensing in CNNM, a putative magnesium transporter. *Structure* 28, 324–335 e324.
- Corral-Rodriguez, M.A., Stuiver, M., Abascal-Palacios, G., Diercks, T., Oyenarte, I., Ereno-Orbea, J., de Opakua, A.I., Blanco, F.J., Encinar, J.A., Spiwok, V., et al. (2014). Nucleotide binding triggers a conformational change of the CBS module of the magnesium transporter CNNM2 from a twisted towards a flat structure. *Biochem. J.* 464, 23–34.
- de Baaij, J.H., Stuiver, M., Meij, I.C., Lainez, S., Kopplin, K., Venselaar, H., Muller, D., Bindels, R.J., and Hoenderop, J.G. (2012). Membrane topology and intracellular processing of cyclin M2 (CNNM2). *J. Biol. Chem.* 287, 13644–13655.
- Funato, Y., Furutani, K., Kurachi, Y., and Miki, H. (2018a). CrossTalk proposal: CNNM proteins are  $Na^+$ / $Mg^{2+}$  exchangers playing a central role in transepithelial  $Mg^{2+}$  (re)absorption. *J. Physiol.* 596, 743–746.
- Funato, Y., Furutani, K., Kurachi, Y., and Miki, H. (2018b). Rebuttal from yosuke Funato, kazuharu furutani, yoshihisa kurachi and hiroaki miki. *J. Physiol.* 596, 751.
- Funato, Y., and Miki, H. (2019). Molecular function and biological importance of CNNM family  $Mg^{2+}$  transporters. *J. Biochem.* 165, 219–225.
- Funato, Y., Yamazaki, D., and Miki, H. (2017). Renal function of cyclin M2  $Mg^{2+}$  transporter maintains blood pressure. *J. Hypertens.* 35, 585–592.
- Funato, Y., Yamazaki, D., Mizukami, S., Du, L., Kikuchi, K., and Miki, H. (2014). Membrane protein CNNM4-dependent  $Mg^{2+}$  efflux suppresses tumor progression. *J. Clin. Invest.* 124, 5398–5410.
- Gimenez-Mascarell, P., Gonzalez-Recio, I., Fernandez-Rodriguez, C., Oyenarte, I., Muller, D., Martinez-Chantar, M.L., and Martinez-Cruz, L.A. (2019). Current structural knowledge on the CNNM family of magnesium transport mediators. *Int. J. Mol. Sci.* 20, 1135.
- Giménez-Mascarell, P., Oyenarte, I., González-Recio, I., Fernández-Rodríguez, C., Corral-Rodríguez, M., Campos-Zarraga, I., Simón, J., Kostantin, E., Hardy, S., Díaz Quintana, A., et al. (2019). Structural insights into the intracellular region of the human magnesium transport mediator CNNM4. *Int. J. Mol. Sci.* 20, 6279.
- Giménez-Mascarell, P., Oyenarte, I., Hardy, S., Breiderhoff, T., Stuiver, M., Kostantin, E., Diercks, T., Pey, A.L., Ereño-Orbea, J., Martínez-Chantar, M.L., et al. (2017). Structural basis of the oncogenic interaction of phosphatase PRL-1 with the magnesium transporter CNNM2. *J. Biol. Chem.* 292, 786–801.
- Göttle, M., Dove, S., Steindel, P., Shen, Y., Tang, W.J., Geduhn, J., König, B., and Seifert, R. (2007). Molecular analysis of the interaction of Bordetella pertussis adenyl cyclase with fluorescent nucleotides. *Mol. Pharmacol.* 72, 526–535.
- Gulerez, I., Funato, Y., Wu, H., Yang, M., Kozlov, G., Miki, H., and Gehring, K. (2016). Phosphocysteine in the PRL-CNNM pathway mediates magnesium homeostasis. *EMBO Rep.* 17, 1890–1900.
- Hardy, S., Uetani, N., Wong, N., Kostantin, E., Labbé, D.P., Bégin, L.R., Mes-Masson, A., Miranda-Saavedra, D., and Tremblay, M.L. (2015). The protein tyrosine phosphatase PRL-2 interacts with the magnesium transporter CNNM3 to promote oncogenesis. *Oncogene* 34, 986–995.
- Hirata, Y., Funato, Y., Takano, Y., and Miki, H. (2014).  $Mg^{2+}$ -dependent interactions of ATP with the cystathionine-beta-synthase (CBS) domains of a magnesium transporter. *J. Biol. Chem.* 289, 14731–14739.

- Hmiel, S.P., Snavely, M.D., Florer, J.B., Maguire, M.E., and Miller, C.G. (1989). Magnesium transport in *Salmonella typhimurium*: genetic characterization and cloning of three magnesium transport loci. *J. Bacteriol.* *171*, 4742–4751.
- Huang, Y., Jin, F., Funato, Y., Xu, Z., Zhu, W., Wang, J., Sun, M., Zhao, Y., Yu, Y., Miki, H., et al. (2021). Structural basis for the Mg<sup>2+</sup> recognition and regulation of the CorC Mg<sup>2+</sup> transporter. *Sci. Adv.* *7*, eabe6140.
- Kostantin, E., Hardy, S., Valinsky, W.C., Kompatscher, A., de Baaij, J.H., Zolotarov, Y., Landry, M., Uetani, N., Martínez-Cruz, L.A., Hoenderop, J.G., et al. (2016). Inhibition of PRL-2-CNNM3 protein complex formation decreases breast cancer proliferation and tumor growth. *J. Biol. Chem.* *291*, 10716–10725.
- Lee, D.D., Galera-Laporta, L., Bialecka-Fornal, M., Moon, E.C., Shen, Z., Briggs, S.P., Garcia-Ojalvo, J., and Süel, G.M. (2019). Magnesium flux modulates ribosomes to increase bacterial survival. *Cell* *177*, 352–360.e313.
- Ni, Q., Shaffer, J., and Adams, J.A. (2000). Insights into nucleotide binding in protein kinase A using fluorescent adenosine derivatives. *Protein Sci.* *9*, 1818–1827.
- Parry, D.A., Mighell, A.J., El-Sayed, W., Shore, R.C., Jalili, I.K., Dollfus, H., Bloch-Zupan, A., Carlos, R., Carr, I.M., Downey, L.M., et al. (2009). Mutations in CNNM4 cause Jalili syndrome, consisting of autosomal-recessive cone-rod dystrophy and amelogenesis imperfecta. *Am. J. Hum. Genet.* *84*, 266–273.
- Polok, B., Escher, P., Ambresin, A., Chouery, E., Bolay, S., Meunier, I., Nan, F., Hamel, C., Munier, F.L., Thilo, B., et al. (2009). Mutations in CNNM4 cause recessive cone-rod dystrophy with amelogenesis imperfecta. *Am. J. Hum. Genet.* *84*, 259–265.
- Stuiver, M., Láinez, S., Will, C., Terry, S., Günzel, D., Debaix, H., Sommer, K., Kopplin, K., Thumfart, J., Kampik, N.B., et al. (2011). CNNM2, encoding a basolateral protein required for renal Mg<sup>2+</sup> handling, is mutated in dominant hypomagnesemia. *Am. J. Hum. Genet.* *88*, 333–343.
- Trachsel, E., Redder, P., Linder, P., and Armitano, J. (2019). Genetic screens reveal novel major and minor players in magnesium homeostasis of *Staphylococcus aureus*. *PLoS Genet.* *15*, e1008336.
- Wang, K., Preisler, S.S., Zhang, L., Cui, Y., Missel, J.W., Grønberg, C., Gotfryd, K., Lindahl, E., Andersson, M., Calloe, K., et al. (2019). Structure of the human ClC-1 chloride channel. *PLoS Biol.* *17*, e3000218.
- Yaginuma, H., Kawai, S., Tabata, K.V., Tomiyama, K., Kakizuka, A., Komatsuzaki, T., Noji, H., and Imamura, H. (2014). Diversity in ATP concentrations in a single bacterial cell population revealed by quantitative single-cell imaging. *Sci. Rep.* *4*, 6522.
- Yamazaki, D., Funato, Y., Miura, J., Sato, S., Toyosawa, S., Furutani, K., Kurachi, Y., Omori, Y., Furukawa, T., Tsuda, T., et al. (2013). Basolateral Mg<sup>2+</sup> extrusion via CNNM4 mediates transcellular Mg<sup>2+</sup> transport across epithelia: a mouse model. *PLoS Genet.* *9*, e1003983.
- Zhang, H., Kozlov, G., Li, X., Wu, H., Gulerez, I., and Gehring, K. (2017). PRL3 phosphatase active site is required for binding the putative magnesium transporter CNNM3. *Sci. Rep.* *7*, 48.

**iScience, Volume 24**

**Supplemental information**

**Identification and mechanistic**

**analysis of an inhibitor**

**of the CorC Mg<sup>2+</sup> transporter**

**Yichen Huang, Kaijie Mu, Xinyu Teng, Yimeng Zhao, Yosuke Funato, Hiroaki Miki, Weiliang Zhu, Zhijian Xu, and Motoyuki Hattori**

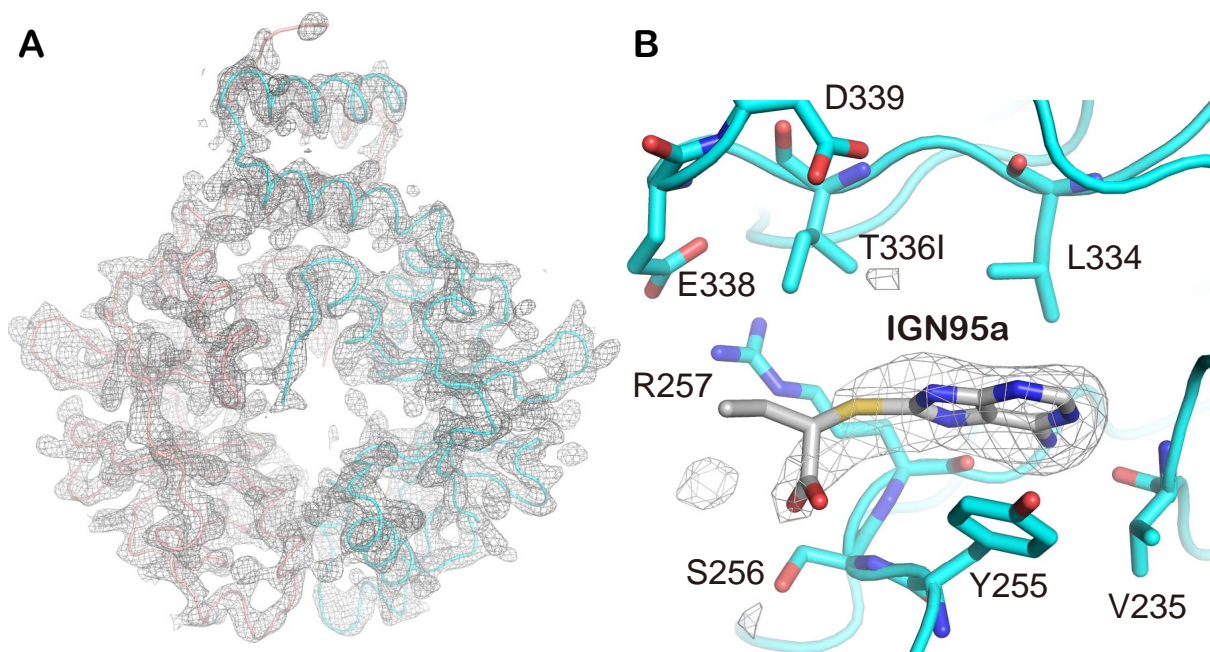


**Figure S1. Electron density maps for the IGN95a-bound structure, Related to Figure 5.**

(**A**) The  $2F_o-F_c$  electron density maps for the overall structure of the IGN95a-bound CBS domain are contoured at  $1 \sigma$ , and are shown in grey mesh. (**B**) The POLDER-OMIT maps for IGN95a are contoured at  $3.0 \sigma$ , and are shown in grey mesh.

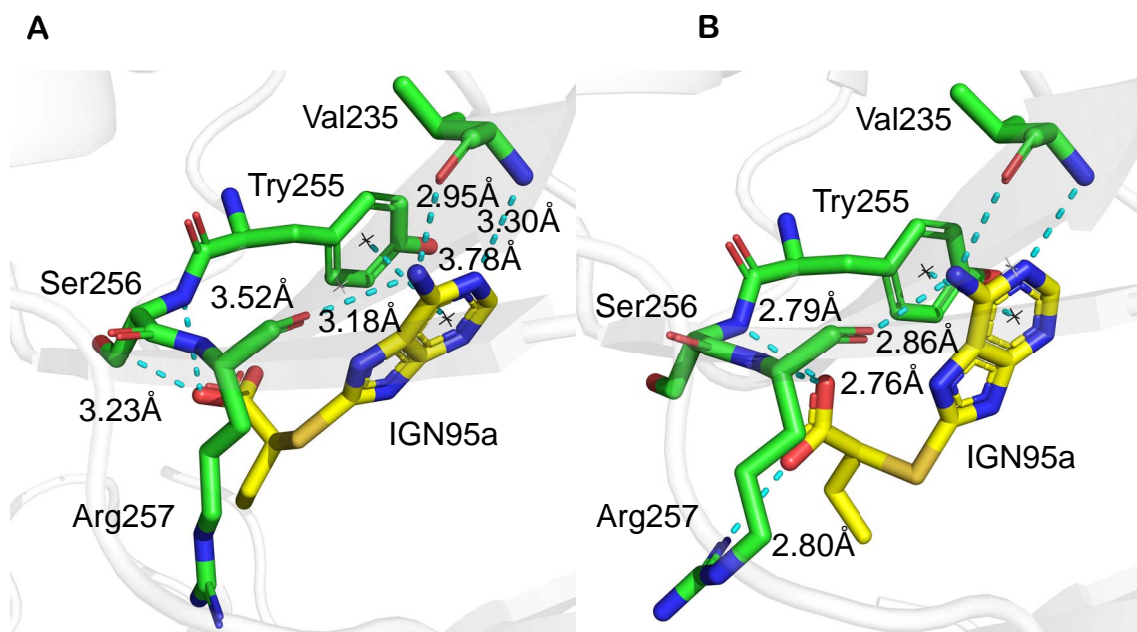


**Figure S2. Comparison of the IGN95a-bound CorC CBS domain structure and the corresponding docking model from virtual screening, Related to Figure 5.**

(A) The binding pose of IGN95a with TpCorC in the crystal structure. (B) The docking pose of IGN95a against TpCorC. The proteins are shown in grey cartoon, the ligands in yellow sticks, and key residues in green sticks. The non-covalent interactions shown as cyan dotted lines with the distance in Å.

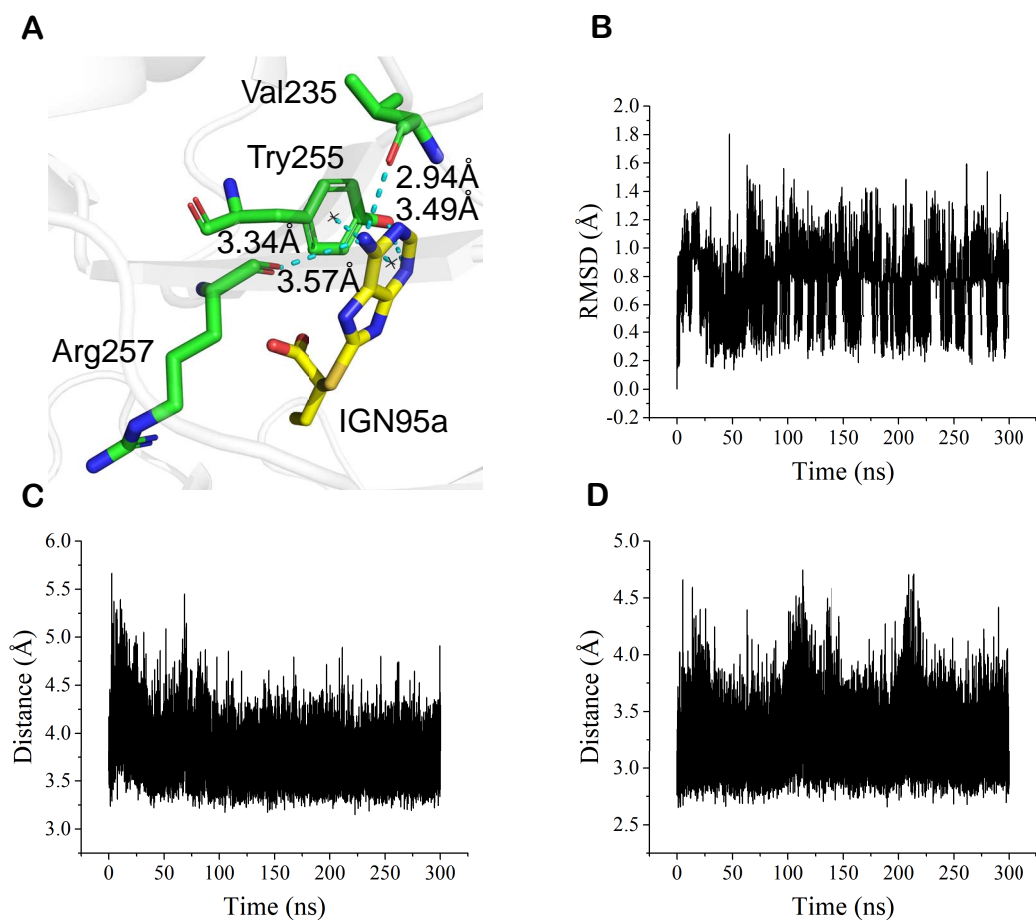


**Figure S3. MD simulations, Related Figure 5.**

(A) The interactions between IGN95a (green sticks) and protein residues (yellow sticks) of the representative conformation during 300 ns trajectories. (B) The RMSDs to the initial structure of IGN95a during 300 ns MD simulations. (C) Distances between the benzene ring of IGN95a and the indole ring of Tyr255 during 300 ns MD simulations. (D) Distances between the amino nitrogen of IGN95a and the carbonyl oxygen of Val235 during 300 ns MD simulations.

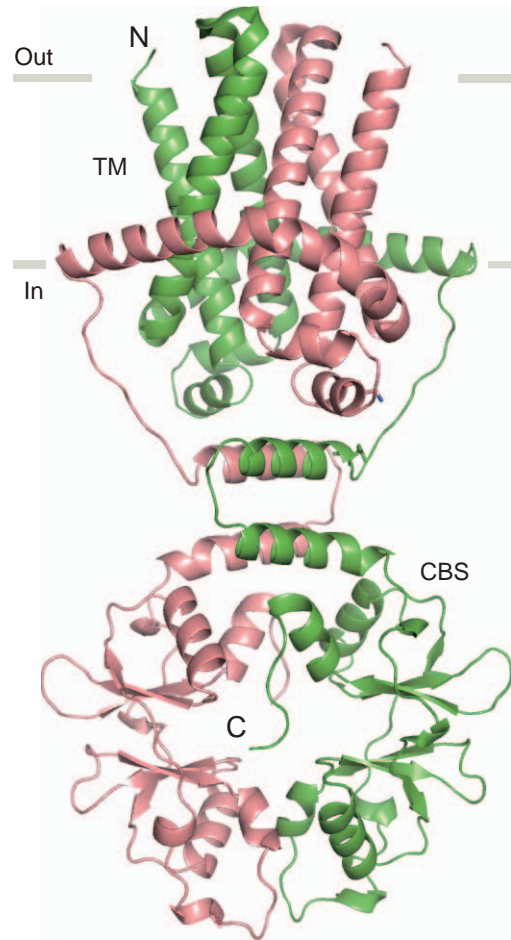


**Figure S4. Structural model of TpCorC TM-CBS, Related to Figure 7.**

Viewed parallel to the membrane. The model was previously reported based on chemical cross-linking experiments and MD simulations. The two subunits are coloured red and green.

**Table S1. ITC statistics, Related to Figure 5.**

<b>TpCorC CBS with IGN95a</b>	<b>n</b>	<b><math>\Delta H^\circ</math> (kcal/mol)</b>	<b><math>-T\Delta S^\circ</math> (kcal/mol)</b>	<b><math>\Delta G^\circ</math> (kcal/mol)</b>	<b><math>K_D</math> (<math>\mu\text{M}</math>)</b>
WT	$0.23 \pm 0.01$	$-6.7 \pm 1.2$	0.8	$-5.9 \pm 1.2$	$46.95 \pm 4.23$
T336I	$0.25 \pm 0.10$	$-18.2 \pm 8.3$	12.9	$-5.3 \pm 8.3$	$147.28 \pm 18.35$
Y255A					ND
<b>CNNM CBS with IGN95a</b>	<b>n</b>	<b><math>\Delta H^\circ</math> (kcal/mol)</b>	<b><math>-T\Delta S^\circ</math> (kcal/mol)</b>	<b><math>\Delta G^\circ</math> (kcal/mol)</b>	<b><math>K_D</math> (<math>\mu\text{M}</math>)</b>
HsCNNM2					>1000
HsCNNM4					> 500

**Table S2.** X-ray Data collection and refinement statistics, Related to Figure 5.

CorC CBS with IGN95a	
<b>Data collection</b>	
Wavelength (Å)	0.9792
Space group	C2
Cell dimensions	
<i>a</i> , <i>b</i> , <i>c</i> (Å)	91.0, 60.5, 82.3
$\alpha$ , $\beta$ , $\gamma$ (°)	90.0, 93.8, 90.0
Resolution (Å)*	45.41 – 2.90 (3.08 – 2.90)
$R_{\text{sym}}$ *	0.157 (1.616)
$I/\sigma I$ *	9.28 (1.09)
Completeness (%)*	99.6 (98.6)
Redundancy*	6.8 (7.1)
$CC_{1/2}$ (%)*	99.7 (52.4)
<b>Refinement</b>	
Resolution (Å)	2.9
No. reflections	19225
$R_{\text{work}}/R_{\text{free}}$	0.210/0.276
No. atoms	
Protein	2445
Ligand/ion	45
Water	14
B-factors	
Protein	75.6
Ligand/ion	90.4
Water	66.0
R.m.s deviations	
Bond lengths (Å)	0.010
Bond angles (°)	1.330
Ramachandran plot	
Favoured (%)	93.2
Allowed (%)	6.9
Outliers (%)	0

\*Highest resolution shell is shown in parenthesis.

**Table S3 Customized parameters for molecular docking, Related to Table 1.**

Parameters	Weights
gauss (o=0, w=0.5, _c=8)	-0.035579
gauss (o=3, _w=2, _c=8)	-0.005156
repulsion (o=0, _c=8)	0.26360521
hydrophobic (g=0.5, _b=1.5, _c=8)	-0.035069
non_dir_h_bond (g=-0.7, _b=0, _c=8)	-0.587439
num_tors_div	1.923
atom_type_gaussian(t1=Magnesium,t2=OxygenXSAcceptor,o=0, w=3, c=8)	-0.3

## Transparent Methods

### STAR METHODS

#### KEY RESOURCES TABLE

REAGENT or RESOURCE	SOURCE	IDENTIFIER
Bacterial and Virus Strains		
<i>Escherichia coli</i> , Rosetta (DE3)	Sigma-Aldrich	Cat# 70954
Chemicals, Peptides, and Recombinant Proteins		
Magnesium Green	Thermo Fisher Scientific	Cat# M3735
TpCorC 183-361, C282A/T336I	This paper	N/A
TpCorC 183-361, C282A	This paper	N/A
TpCorC 183-361, C282A/Y255A	This paper	N/A
HsCNNM2 433-584	This paper	N/A
HsCNNM4 360-511	This paper	N/A
TpCorC 23-441, C282A/T106C	This paper	N/A
TpCorC 23-441, C282A/T106C/Y255A/T336I	This paper	N/A
Apyrase	Sigma-Aldrich	Cat# A6535
ATP	Sigma-Aldrich	Cat# A7699
Polyethylene glycol 400	Molecule Dimensions	Cat# MD2-250-3
CuSO <sub>4</sub>	Sangon Biotech	Cat# A100330
Bis-1,10-phenanthroline	Sangon Biotech	Cat# A600693
Mant-ATP	Sigma-Aldrich	Cat# 18723
IGN95a	WuXi AppTec	N/A
IGN23	Topscience Co., Ltd	N/A
IGN19	Topscience Co., Ltd	N/A
Deposited Data		

TpCorC CBS <sup>C282A/T336I</sup> -IGN95a	This paper	PDB: 7CFI
Experimental Models: Cell Lines		
HEK293	Funato et al., 2014	NA
Recombinant DNA		
pET28b-TpCorC 183-361 C282A	Huang et al., 2021	NA
pET28b-TpCorC 183-361 C282A/Y255A	Huang et al., 2021	NA
pET28b-TpCorC 183-361 C282A/T336I	Huang et al., 2021	NA
pET28b- HsCNNM2 433-584	This paper	NA
pET28b- HsCNNM4 360-511	This paper	NA
pET25b-TpCprC 23-441 C282A/T106C	Huang et al., 2021	NA
pET25b-TpCprC 23-441 C282A/T106C/Y255A/T336I	This paper	NA
pCMV tag 4A-SpCNNM4(1-178)-TpCorC	Huang et al., 2021	NA
Software and Algorithms		
Prism (version 6.07)	GraphPad	<a href="http://www.graphpad.com">http://www.graphpad.com</a>
smina	Koes et al. 2013	<a href="https://sourceforge.net/projects/smina/">https://sourceforge.net/projects/smina/</a>
Amber16	Salomon-Ferrer et al., 2013	<a href="https://ambermd.org/">https://ambermd.org/</a>
MGLTools 1.5.6	Morris, et al. 2009	<a href="http://mgltools.scripps.edu/">http://mgltools.scripps.edu/</a>
PyMOL	Schrödinger, LLC.	<a href="https://pymol.org/">https://pymol.org/</a>
XDS	Kabsch et al. 2010	<a href="http://xds.mpimf-heidelberg.mpg.de/">http://xds.mpimf-heidelberg.mpg.de/</a>
ZOO	Hirata et al., 2019	<a href="https://github.com/keitaroyam/yamtbx">https://github.com/keitaroyam/yamtbx</a>
KAMO	Yamashita et al., 2018	<a href="https://github.com/keitaroyam/yamtbx">https://github.com/keitaroyam/yamtbx</a>
Phenix	Liebschner et al., 2019	<a href="http://www.phenix-online.org/">http://www.phenix-online.org/</a>
Coot	Emsley et al., 2010	<a href="https://www.ccp4.ac.uk/">https://www.ccp4.ac.uk/</a>

Other		

## **METHODS DETAILS**

### **Protein expression and purification**

The CBS domain constructs of the CorC gene from *Thermus parvatiensis* (accession ID: WP\_060384576.1) (residues 183-361, C282A) and its mutants were expressed and purified as described previously (Huang et al., 2021). In brief, CBS domain constructs with a human rhinovirus (HRV) 3C protease cleavage site and an octa-histidine tag were transformed into the *Escherichia coli* Rosetta (DE3) strain. *E. coli* cells were cultured in LB medium containing 30 µg/ml kanamycin at 37 °C to an OD600 of 0.6, and then, expression was induced with IPTG at a final concentration of 0.5 mM. The *E. coli* cells were then cultured at 37 °C for another 3 hours and harvested by centrifugation (5,000 ×g, 15 minutes). After cell disruption with buffer A [150 mM NaCl, 50 mM Tris (pH 8.0) with 1 mM phenylmethanesulphonyl fluoride (PMSF)], the cell lysate was centrifuged (20,000 ×g, 1 hour). The supernatant was incubated with TALON resin (Takara, Japan) equilibrated with buffer A for 1 hour. The resin was then washed with buffer A containing 10 mM imidazole and eluted with buffer A containing 300 mM imidazole. A His-tagged HRV 3C protease was then added to the eluate to cleave the histidine tag, followed by dialysis with buffer A overnight. The digested sample was reapplied to TALON resin preequilibrated with buffer A. The flow-through fractions from the resin were concentrated by an Amicon Ultra 30K filter (Merck Millipore,

USA) and applied to a Superdex 75 Increase 10/300 column (GE Healthcare, USA) in buffer B (100 mM NaCl, 20 mM HEPES (pH 7.5)) for size-exclusion chromatography. The main fractions were collected and concentrated to 10 mg/ml. The CBS domain constructs of human CNNM2 (accession ID: NP\_060119.3, residues 433-584) and CNNM4 (accession ID: NP\_064569.3, residues 360-511) were similarly expressed and purified.

The C282A and cysteine substitution mutants of TpCorC (residues 23-441) were purified for biochemical cross-linking experiments, as described previously (Huang et al., 2021). In addition to the previous purification protocol, to remove endogenous ATP from the purified protein, additional dialysis was performed before solubilization. The collected membrane fraction was transferred into a 10 kDa Spectra/Por 6 dialysis membrane Spectra/Por 6 (Spectrum, USA) and dialyzed against buffer C (1 M NaCl, 50 mM Tris (pH 9.5), 5% glycerol, 2 mM  $\beta$ -ME) for four days by changing buffer C once a day at 4 °C. After 4 days, the membrane was further dialyzed against buffer A containing 2 mM  $\beta$ -ME for 3 hours. In addition, apyrase (Sigma, USA) was added at 0.5 units/ml during cell disruption and membrane solubilization.

## **Crystallization**

Before crystallization, the crystallization construct of the TpCorC CBS domain (residues 183-361, C282A and T336I) was mixed with IGN95a at a final concentration of 2.5 mM. For crystallization using the vapour diffusion method, 1  $\mu$ l of the TpCorC CBS domain protein was mixed with 1  $\mu$ l of reservoir solution (0.1 M KCl, 0.1 M MES (pH 6.0), 32% w/v PEG 400) and stored at 18 °C. Before flash freezing in liquid

nitrogen, crystals were incubated with the cryoprotectant solution (0.1 M KCl, 0.1 M MES (pH 6.0), 40% PEG 400, 5 mM IGN95a) for 1 hour and then harvested.

### **Data collection and structure determination**

X-ray diffraction data sets were collected at the SSRF beamline BL17U1 and the SPring-8 beamline BL32XU and processed using XDS (Kabsch, 2010). Notably, at the SPring-8 beamline BL32XU, the X-ray diffraction data sets were collected and processed with the assistance of the automated data collection system ZOO (Hirata et al., 2019) and the automatic data processing system KAMO (Yamashita et al., 2018).

The structure of the TpCorC CBS domain construct in complex with IGN95a (residues 183-361, C282A and T336I) was determined by molecular replacement with Phaser using the previously determined TpCorC CBS domain structure (PDB ID: 7CFI). The structure was further manually rebuilt with Coot (Emsley et al., 2010) and refined by Phenix (Liebschner et al., 2019). The Ramachandran plots were calculated using MolProbity (Chen et al., 2010). The statistics of data collection and refinement are shown in **Table S2**. All structure figures were generated with PyMOL (<https://pymol.org/>). The 2D interaction diagram between IGN95a and the CorC CBS domain in **Figure 5C** was generated with LigPLot+ (Laskowski and Swindells, 2011).

### **Isothermal titration calorimetry**

All ITC measurements were conducted using a MicroCal ITC200 (GE Healthcare, USA) at 25 °C. For ITC experiments, the CorC CBS domain, its mutants and CNNM2 and CNNM4 CBS domain proteins were purified as similarly described above, but

buffer D (100 mM KCl, 5 mM MgCl<sub>2</sub>, and 20 mM HEPES (pH 7.5)) was used for size-exclusion chromatography. IGN95a was dissolved in 100% DMSO at a concentration of 100 mM and further diluted to 1 mM with buffer D for ITC experiments. A total of 250 µl of purified proteins (100 µM) was applied to the thermally equilibrated ITC cell. The ligand syringe was filled with 40 µl of IGN95a solution. The ligands were injected 20 times (0.5 µl for injection 1 and 2 µl for injections 2-20), with 120 s intervals between injections. The background data obtained from buffer D containing 1% DMSO were subtracted before data analysis. The data were analysed with Microcal Origin software. Measurements were performed at least twice, and similar results were obtained. The data statistics are summarized in **Table S1**.

### **Biochemical cross-linking**

A total of 4.0 µl of 20 µM TpCorC protein in 20 mM HEPES (pH 7.5) containing 0.03% n-dodecyl-β-D-maltopyranoside (DDM) (Anatrace, USA) and either 150 mM NaCl or 150 mM KCl was mixed with 0.5 µl of 2 mM EDTA, 2 mM EDTA+ 20 mM ATP, 2 mM EDTA+ 20 mM IGN95a, 100 mM MgCl<sub>2</sub> or Milli-Q water and then incubated for 1 hour at 4 °C. Then, 0.5 µl of the reaction solution (5 mM Cu<sup>2+</sup> bis-1,10-phenanthroline in a 1:3 molar ratio) or Milli-Q water was added, followed by incubation for 15 minutes at 4 °C. The samples were analysed by non-reducing SDS-PAGE. Experiments were performed at least twice, and similar results were obtained.

### **IGN95a**

IGN95 (CAS No. 436086-77-0) with a chiral centre was originally purchased from

Topsience Co., Ltd. The S-configuration of IGN95 (IGN95a) was separated by WuXi AppTec. The high-performance liquid chromatography (HPLC) purity of IGN95a was greater than 96%. The calculated miLogP was 1.26 (<https://www.molinspiration.com/cgi-bin/properties>), indicating the cell membrane permeability of IGN95a.

## Molecular docking

A total of 6412 in-house compounds (mostly from commercial databases, e.g., Specs, Maybridge, and ChemDiv, and some synthesized at the Drug Discovery and Design Center, CAS) in pdbqt format were docked to the TpCorC CBS domain by smina (Koes et al., 2013), which is a branch of AutoDock Vina (Trott and Olson, 2010) with improved scoring and minimization. Only chain A of the CBS domain (PDB ID: 7CFI) was used for docking, Mg<sup>2+</sup> ions interacting with the phosphate group of ATP were preserved, and all water molecules were removed. The hydrogens were added to the CBS domain by pdb2pqr (--ff=amber --ffout=amber --chain --with-ph=7) (Dolinsky et al., 2004). Then, the model was converted to pdbqt format by the prepare\_receptor4.py script in MGLTools version 1.5.6 (Morris et al., 2009). The geometrical centre of the ATP ligand in the crystal structure was used to define the grid centre, and the grid size was set to 15.0 Å. The random seed was explicitly set to 0. The exhaustiveness of the global search was set to 32, and at most 1 binding mode was generated for each compound. A custom Vina scoring function (**Table S3**) was used in this study (Shi et al., 2020). The ligand efficiency was calculated as the ratio of the docking score to the number of non-hydrogen atoms in the compound.

## **Molecular dynamics simulation of the CBS domain with chemical compounds**

Each docking complex or the crystal structure was immersed in a cubic box of TIP3P water that was extended by 9 Å from the solute, and counter ions of Na<sup>+</sup> or Cl<sup>-</sup> were added to neutralize the system. The compound and protein were parameterized by the general Amber force field (GAFF) (Wang et al., 2004) and Amber ff03 force field (Duan et al., 2003), respectively. Ten thousand steps of minimization with constraints (10 kcal/mol/Å<sup>2</sup>) on the heavy atoms of the complex, including 5,000 steps of steepest descent minimization and 5,000 steps of conjugate gradient minimization, were used to optimize each system. Then, each system was heated to 300 K within 0.2 ns, followed by a 0.1 ns equilibration in the NPT ensemble. Finally, 5 ns MD simulations on the docking complex at 300 K were performed for the MM/GBSA calculations. To assess the binding stability of the crystal structure of the TpCorC CBS domain complexed with IGN95a, a 300 ns MD simulation was conducted. Minimization, heating and equilibration were performed with the Sander program in Amber16. The 5 ns or 300 ns production run was performed with *pmemd.cuda*.

### **Binding free energy calculation**

Based on the first 5 ns of the MD simulation trajectories, the binding free energy ( $\Delta G$ ) was calculated with MM/GBSA (Kollman et al., 2000; Srinivasan et al., 1998) according to equation (1):

$$\Delta G = \Delta H - T\Delta S = \Delta E_{\text{ele}} + \Delta E_{\text{VDW}} + \Delta G_{\text{gb}} + \Delta G_{\text{np}} - T\Delta S \quad (1)$$

where  $\Delta E_{\text{ele}}$  and  $\Delta E_{\text{VDW}}$  refer to the electrostatic and van der Waals energy terms, respectively, and  $\Delta G_{\text{gb}}$  and  $\Delta G_{\text{np}}$  refer to polar and non-polar solvation free energies, respectively. Conformational entropy ( $T\Delta S$ ) was calculated by the nmode module in Amber16. The dielectric constants for the solvent and solute were set to 80.0 and 1.0, respectively, and the OBC solvation model (igb = 5 and PBradii = 5) (Onufriev et al., 2004) was used in this study. Other parameters were set to default values.

### **Mant-ATP binding assay**

The mant-ATP binding assay was conducted in buffer E [50 mM Tris (pH 8.0), 150 mM NaCl and 0.03% DDM]. For saturation binding experiments, a final concentration of 1  $\mu\text{M}$  TpCorC CBS domain protein was mixed with mant-ATP at the indicated concentrations in 96-well plates and incubated in the dark at RT for 1 hour. For ATP-based inhibition experiments, a final concentration of 1  $\mu\text{M}$  TpCorC CBS domain protein and 1  $\mu\text{M}$  mant-ATP were mixed with ATP at the indicated concentrations. To test the effects of chemical compounds, 1 and 5  $\mu\text{M}$  TpCorC CBS protein was preincubated with 0.25 mM and 2 mM chemical compounds, followed by the addition of 1 and 5  $\mu\text{M}$  mant-ATP, as shown in **Figures 3C and 3D**, respectively, whereas the control samples included the same concentration of DMSO. FRET from endogenous Trp residues to bound mant-fluorophore was measured (Göttle et al., 2007; Ni et al., 2000). The fluorescence intensity was measured in an experimental setup with excitation at 280 nm and emission at 450 nm with Cytation 3 (BioTek).

The FRET intensity was calculated by equation (2).

$$I_{\text{FRET}} = I_{A\text{-raw}} - D_{\text{leakage}} - A_{\text{direct}} \quad (2)$$

$I_{A-raw}$  is the intensity measured at 450 nm with 280 nm excitation,  $D_{leakage}$  is the leakage of the donor emission into the acceptor wavelength (450 nm) upon donor excitation, and  $A_{direct}$  is the direct excitation of the acceptor with the donor wavelength (280 nm).

### **Mg<sup>2+</sup> export assay**

The Mg<sup>2+</sup> export assay of TpCorC was performed as described previously (Huang et al., 2021). In brief, HEK293-derived cell lines stably expressing TpCorC containing the membrane targeting sequence from human CNNM4 (residues 1-178) were cultured in DMEM (Nissui, Japan) supplemented with 10% FBS, antibiotics and 40 mM Mg<sup>2+</sup> until used for the Mg<sup>2+</sup> export assay. The effects of 40 mM MgCl<sub>2</sub> on cellular metal homeostasis and signaling has been examined in previous studies (Funato et al., 2014; Yamazaki et al., 2013). The Mg<sup>2+</sup> export assay using Magnesium Green was performed as described previously (Yamazaki et al., 2013). Mg<sup>2+</sup> loading was performed for 45 minutes at 37°C in all measurements, and all buffers used were adjusted to 295-305 mOsm, as in the previous experiments (Yamazaki et al., 2013). The data are shown as either line graphs indicating the time course of mean relative fluorescent intensities or as bar graphs of mean relative fluorescent intensities 5 minutes after Mg<sup>2+</sup> depletion. Relative fluorescence intensities were estimated as the ratio of fluorescence intensity at time 5 minutes to that at time zero. After imaging analyses, HEK293 cells were fixed with PBS containing 3.7% formaldehyde and examined by immunofluorescence microscopy to check protein expression. Statistical analyses were conducted using GraphPad Prism 6 software (GraphPad Software). The data are shown as the mean ± SEM. The *p*-values were calculated by 1-way ANOVA with Holm-Sidak post hoc tests.

## **Supplemental References**

Chen, V.B., Arendall, W.B., 3rd, Headd, J.J., Keedy, D.A., Immormino, R.M., Kapral, G.J., Murray, L.W., Richardson, J.S., and Richardson, D.C. (2010). MolProbity: all-atom structure validation for macromolecular crystallography. *Acta crystallographica Section D, Biological crystallography* 66, 12-21.

Dolinsky, T.J., Nielsen, J.E., McCammon, J.A., and Baker, N.A. (2004). PDB2PQR: an automated pipeline for the setup of Poisson-Boltzmann electrostatics calculations. *Nucleic Acids Res* 32, W665-667.

Duan, Y., Wu, C., Chowdhury, S., Lee, M.C., Xiong, G., Zhang, W., Yang, R., Cieplak, P., Luo, R., Lee, T., *et al.* (2003). A point-charge force field for molecular mechanics simulations of proteins based on condensed-phase quantum mechanical calculations. *Journal of computational chemistry* 24, 1999-2012.

Emsley, P., Lohkamp, B., Scott, W.G., and Cowtan, K. (2010). Features and development of Coot. *Acta crystallographica Section D, Biological crystallography* 66, 486-501.

Funato, Y., Yamazaki, D., Mizukami, S., Du, L., Kikuchi, K., and Miki, H. (2014). Membrane protein CNNM4-dependent Mg<sup>2+</sup> efflux suppresses tumor progression. *The Journal of clinical investigation* 124, 5398-5410.

Göttle, M., Dove, S., Steindel, P., Shen, Y., Tang, W.J., Geduhn, J., König, B., and Seifert, R. (2007). Molecular analysis of the interaction of *Bordetella pertussis* adenylyl cyclase with fluorescent nucleotides. *Molecular pharmacology* 72, 526-535.

Hirata, K., Yamashita, K., Ueno, G., Kawano, Y., Hasegawa, K., Kumasaka, T., and

Yamamoto, M. (2019). ZOO: an automatic data-collection system for high-throughput structure analysis in protein microcrystallography. *Acta Crystallographica Section D* 75, 138-150.

Huang, Y., Jin, F., Funato, Y., Xu, Z., Zhu, W., Wang, J., Sun, M., Zhao, Y., Yu, Y., Miki, H., *et al.* (2021). Structural basis for the Mg<sup>2+</sup> recognition and regulation of the CorC Mg<sup>2+</sup> transporter. *Science advances* 7, eabe6140.

Kabsch, W. (2010). XDS. *Acta Crystallographica Section D* 66, 125-132.

Koes, D.R., Baumgartner, M.P., and Camacho, C.J. (2013). Lessons learned in empirical scoring with smina from the CSAR 2011 benchmarking exercise. *Journal of chemical information and modeling* 53, 1893-1904.

Kollman, P.A., Massova, I., Reyes, C., Kuhn, B., Huo, S., Chong, L., Lee, M., Lee, T., Duan, Y., Wang, W., *et al.* (2000). Calculating structures and free energies of complex molecules: combining molecular mechanics and continuum models. *Accounts of chemical research* 33, 889-897.

Laskowski, R.A., and Swindells, M.B. (2011). LigPlot+: multiple ligand-protein interaction diagrams for drug discovery. *Journal of chemical information and modeling* 51, 2778-2786.

Liebschner, D., Afonine, P.V., Baker, M.L., Bunkoczi, G., Chen, V.B., Croll, T.I., Hintze, B., Hung, L.-W., Jain, S., McCoy, A.J., *et al.* (2019). Macromolecular structure determination using X-rays, neutrons and electrons: recent developments in Phenix. *Acta Crystallographica Section D* 75, 861-877.

Morris, G.M., Huey, R., Lindstrom, W., Sanner, M.F., Belew, R.K., Goodsell, D.S., and Olson, A.J. (2009). AutoDock4 and AutoDockTools4: Automated docking with selective receptor flexibility. *Journal of computational chemistry* 30, 2785-2791.

Ni, Q., Shaffer, J., and Adams, J.A. (2000). Insights into nucleotide binding in protein kinase A using fluorescent adenosine derivatives. *Protein science : a publication of the Protein Society* 9, 1818-1827.

Onufriev, A., Bashford, D., and Case, D.A. (2004). Exploring protein native states and large-scale conformational changes with a modified generalized born model. *Proteins* 55, 383-394.

Shi, Y., Zhang, X., Mu, K., Peng, C., Zhu, Z., Wang, X., Yang, Y., Xu, Z., and Zhu, W. (2020). D3Targets-2019-nCoV: a webserver for predicting drug targets and for multi-target and multi-site based virtual screening against COVID-19. *Acta pharmaceutica Sinica B*.

Srinivasan, J., Cheatham, T.E., Cieplak, P., Kollman, P.A., and Case, D.A. (1998). Continuum Solvent Studies of the Stability of DNA, RNA, and Phosphoramidate–DNA Helices. *Journal of the American Chemical Society* 120, 9401-9409.

Trott, O., and Olson, A.J. (2010). AutoDock Vina: improving the speed and accuracy of docking with a new scoring function, efficient optimization, and multithreading. *Journal of computational chemistry* 31, 455-461.

Wang, J., Wolf, R.M., Caldwell, J.W., Kollman, P.A., and Case, D.A. (2004). Development and testing of a general amber force field. *Journal of computational chemistry* 25, 1157-1174.

Yamashita, K., Hirata, K., and Yamamoto, M. (2018). KAMO: towards automated data processing for microcrystals. *Acta Crystallographica Section D* 74, 441-449.

Yamazaki, D., Funato, Y., Miura, J., Sato, S., Toyosawa, S., Furutani, K., Kurachi, Y., Omori, Y., Furukawa, T., Tsuda, T., *et al.* (2013). Basolateral Mg<sup>2+</sup> extrusion via CNNM4 mediates transcellular Mg<sup>2+</sup> transport across epithelia: a mouse model. *PLoS*

Genet 9, e1003983.